Integrative single-cell analysis of neural stem/progenitor cells reveals epigenetically dysregulated interferon response in progressive multiple sclerosis

Bongsoo Park[1*], Alexandra M. Nicaise[2*], Dimitrios Tsitsipatis[3*], Liviu Pirvan[4], Pranathi Prasad[2], Miguel Larraz Lopez De Novales[4], Julia Whitten[1], Luka Culig[1], Joseph Llewellyn[1], Rosana-Bristena Ionescu[2], Cory M. Willis[2], Grzegorz Krzak[2], Jinshui Fan[3], Supriyo De[3], Marta Suarez Cubero[5], Angeliki Spathopoulou[5], Luca Peruzzotti-Jametti[2,6], Tommaso Leonardi[7], Frank Edenhofer[5], Myriam Gorospe[3], Irina Mohorianu[4°], Stefano Pluchino[2°], and Isabel Beerman[1°]

[1]Epigenetics and Stem Cell Unit, Translational Gerontology Branch, National Institute on Aging, NIH, Baltimore, MD, 21224 USA
[2]Department of Clinical Neurosciences and NIHR Biomedical Research Centre, University of Cambridge, Cambridge CB2 0AH, UK
[3]RNA Regulation Section, Laboratory of Genetics and Genomics, National Institute on Aging, NIH, Baltimore, MD, 21224 USA
[4]Wellcome-MRC Cambridge Stem Cell Institute, Jeffrey Cheah Biomedical Centre, University of Cambridge, Cambridge CB2 0AW, UK
[5]Department of Genomics, Stem Cell Biology and Regenerative Medicine & CMBI, Leopold-Franzens-University Innsbruck, Innsbruck, Austria
[6]Department of Metabolism, Digestion and Reproduction, Imperial College London, London SW7 2AZ, UK
[7]Center for Genomic Science of IIT@SEMM, Instituto Italiano di Tecnologia (IIT), 20139 Milan, Italy

[*]These authors contributed equally to this work.

Lead contact: Prof. Stefano Pluchino (SP), Email: spp24@cam.ac.uk

[°]**Corresponding author(s):** Dr Irina Mohorianu, email: iim22@cam.ac.uk; Prof. Stefano Pluchino (SP), Email: spp24@cam.ac.uk; Dr Isabel Beerman, email: isabel.beerman@nih.gov.

SUMMARY

Progressive multiple sclerosis (PMS) is characterized by a primary smouldering pathological disease process associated with a superimposed inflammatory activity. Cellular and molecular processes sustaining the pathobiology of PMS remain to be identified.

We previously discovered senescence signatures in neural stem/progenitor cells (NSCs) from people with PMS. Applying direct reprogramming to generate directly induced NSCs (iNSCs) from somatic fibroblasts, we retain epigenetic information and observe hypomethylation of genes associated with lipid metabolic processes and IFN signalling only in PMS lines. Single-cell/nucleus transcriptomic and epigenetic profiling reveal an inflammatory, senescent-like, IFN-responsive radial glia (RG)-like cell subcluster mainly in PMS iNSCs that is driven by IFN-associated transcription factors. Lastly, we identify a population of senescent, IFN-responsive, disease-associated RG-like cells (DARGs) in the PMS brain that share pseudotime trajectories with iNSCs *in vitro*.

We describe the existence of a non-neurogenic, dysfunctional DARG population that has the potential to fuel smouldering inflammation in PMS.

KEY WORDS

Neural stem/progenitor cells, radial glia, single cell/nuclei multiomics, direct reprogramming, RNA sequencing, DNA methylation, senescence, interferon, epigenetics, progressive multiple sclerosis.

INTRODUCTION

Multiple sclerosis (MS) is a complex neuroinflammatory and neurodegenerative disease characterized by inflammation and demyelination in the central nervous system (CNS). It is believed to be caused by an interplay of genetic predisposition and environmental risk factors, such as exposure to viruses.[1] The early phase of the disease, known as relapsing remitting MS (RRMS), pathologically manifests as acute demyelinating lesions with some endogenous repair. There are disease-modifying therapies (DMTs) available that target peripheral immune cells to reduce the risk of developing new lesions and clinical relapses. Over time, however, most people with RRMS transition into a progressive (PMS) stage of the disease that is characterized by the steady accumulation of neurological disability in the absence of endogenous repair that leads to neurodegeneration. Despite most available DMTs being effective in people with RRMS they are much less effective in people with PMS. This has made the progressive stage of the disease an unmet clinical need.[1]

Pathological, neuroimaging, and clinical data suggest that progressive MS is driven by a primary smouldering process associated with inflammation. Several mechanisms have been proposed to drive smouldering MS, including innate immune activation, demyelination and energy deficits, adaptive immunity, and, recently, age-related mechanisms.[2,3]

Age is one of the most significant risk factors in the development of PMS, which is similar to other neurodegenerative diseases such as Alzheimer's and Parkinson's disease.[4,5] Longitudinal assessment of brain aging using imaging technologies showed that people with MS demonstrate increased '*brain age*' compared to healthy controls that was defined by increased atrophy and decreased grey matter volumes.[6,7] Pathological hallmarks of cellular aging, such as senescence and senescence-associated changes, have been identified in people with PMS. These include decreased telomere length in peripheral leukocytes,[8-10] increased DNA and mitochondrial damage in neurons *in situ,*[11-13] increased epigenetic age in glial cells,[14] senescence-associated secretory phenotype (SASP) in microglia and astrocytes,[15,16] and p16/CDKN2A expression in glia and neural stem/progenitor cells (NSCs).[16,17] The increasing body of evidence suggesting an association of PMS with cellular senescence requires further study to understand how the accumulation of senescent glial cells contributes to disease pathogenesis.

The genetic components underlying MS risk and severity are incredibly complex. Genome wide association studies (GWAS) largely implicated cells of the peripheral immune system in the development of disease. However, mapping of MS susceptibility genes onto brain tissue has revealed enrichment of MS-susceptibility genes in glial cells of the CNS, including astrocytes, oligodendrocytes, and microglia. Moreover, prediction of MS severity from genetic

loci involved in the CNS were found to be associated with mitochondrial function, cellular senescence, and synaptic plasticity.[18]

Recent work with induced pluripotent stem cells (iPSCs), which retain the genetic information from the starting cell and is maintained in the resulting cell type of interest, has allowed for modelling of complex human brain disorders *in vitro*. Although iPSCs offer a powerful platform for modelling of human diseases, epigenetic modifications, especially those associated with aging, are lost in the reprogramming process due to the use of the Yamanaka factors.[19-21] Epigenetic changes, which can be reflected by environmental risk factors such as smoking and exposure to viruses, are likely contribute to MS susceptibility and progression. A few studies have identified aberrant DNA methylation patterns in both CNS tissue and peripheral blood and leukocytes in people with MS. Many of these patterns are associated with functional pathways related to immune response, neuronal survival[22], and demyelination.[23] Recent work has found that iPSC-NSCs from patients with PMS display markers of senescence and prevent oligodendrocyte progenitor cell differentiation via the SASP.[17,24] Furthermore, iPSC-astrocytes from MS patients also display senescence-related gene expression, dysfunctional metabolism, and increased immune and inflammatory genes.[25,26]

Stem cell exhaustion is a known hallmark of biological aging that is typically associated with reduced tissue repair. Adult brain stem cells/NSCs, also known as radial glia-like cells (RG), are astroglial-like cells that classically reside in the mammalian subventricular zone and dentate gyrus of the hippocampus and can give rise to mature neurons, astrocytes, and oligodendrocytes.[27] Furthermore, noncanonical niches for RG have also been reported, including the neocortex of primates,[28] the cerebellum of rabbits,[29] the amygdala of mice,[30] and the striatum of humans.[31] Studies in animals have shown that with progressing age and neurodegenerative disease the capabilities of RGs, such as differentiation into neurons and repair capabilities.[32-34] Many studies have attempted to address the existence, persistence, and role of NSC/RGs in the human brain following early post-natal life. Immunostaining of post-mortem human brains[35] identified NSCs in the lining of the walls of the lateral ventricle, the dentate gyrus, and the olfactory epithelium.[36,37] However, their capacity for neurogenesis and differentiation, as well as their presence outside of the main CNS germinal stem cell niches is much debated.[38,39] More recently, phenomena such as inflammation and injury support both de-maturation of neurons[40] and de-differentiation of astrocytes[41] into NSC/RG-like cell states. NSCs expressing glial markers and displaying features of senescence have also been identified near lesioned areas in post-mortem MS brain tissue.[17,42,43] Their role and putative function in brain physiology and disease is not currently understood.

Disease modelling with stem cell technologies holds the promise for understanding cellular dynamics that were previously unreachable in brain cells *in vivo*. We employed the use of direct reprogramming technology, which better retains epigenetic memory of the donor cells ,[44] to better investigate the origin of the senescent phenotype in NSCs within the context of PMS.[17,24,25,] We directly converted skin-derived fibroblasts from healthy human controls and people with PMS into stably expandable induced NSCs (iNSC). This was done by exposing fibroblasts to a transient (24-hour long) exposure to the Yamanaka factors[45] in the presence of NSC differentiation factors to generate a heterogenous population of stem and progenitor cells.

By subjecting both the parental fibroblasts and iNSCs to whole genome bisulfite sequencing (WGBS), we identified hypomethylated genes encoding proteins that function in pathways similar to those associated with inflammatory and interferon (IFN) signalling in PMS cells, suggesting a predisposition to inflammation. Furthermore, direct reprogramming to iNSCs maintained epigenetic information from the donor cells. Through both bulk and single-cell/ nucleus transcriptomics analyses, we found increased activation of pathways pertaining to cellular senescence, inflammation, and IFN signalling in a subset of PMS iNSCs. Combined single-nuclei ATACseq supported changes in chromatin accessibility and was linked to consistent pathways. Within the heterogenous iNSCs, we identified a focused inflammatory and senescent-like cluster and elevated expression of related upstream transcription factor IRF1 in PMS iNSCs. We integrated published post-mortem single-cell/nuclei transcriptomics data sets and confirmed the presence of non-neurogenic, disease-associated RG-like cells (DARGs) in the PMS brain, primarily in chronic active, slowly expanding lesions, exhibiting senescence and IFN-responsive characteristics.

Our work confirms that direct reprogramming technology is a powerful tool to model disease-in-a-dish to study neurodegenerative disorders. In doing so, it led us to identify the existence of a long-neglected, non-neurogenic DARG cell cluster especially in chronic brain MS lesions that has the potential to fuel continuous smouldering inflammation in PMS.

RESULTS

Bulk (multi-modal) sequencing reveals upregulation of senescence and inflammatory pathways in PMS iNSCs

To model disease and age associated NSC features, we directly reprogrammed skin-derived fibroblasts from control healthy subjects (Ctrl) and people with PMS (PMS) into stably

172 expandable iNSCs (**Table S1**).[45] We confirmed the expression of established and accepted
173 NSC markers, including the mRNAs, using RT-PCR, and proteins, using
174 immunocytochemistry, that encode Nestin (NES), SOX2, ETNPPL, and PAX6, as well as the
175 clearance of Sendai virus markers.[46] PCA summary of transcriptomic signatures across
176 samples (**Fig. 1A**) revealed robust signal across replicates and a clear separation between
177 the Ctrl and PMS samples. Additional checks comprised incremental Jaccard similarity index
178 (**Fig. S1A**),[47] and assessment and removal of technical noise using noisyR (**Fig. S1B**),[48]
179 followed by normalization of expression levels.[47] The differential expression analyses (with
180 convergent results on the DESeq2[49] and edgeR[50] pipelines) led to 1,021 upregulated and 844
181 downregulated genes (FDR < 0.05, $|\log2(FC)| \geq 0.5$) that included transcripts related to
182 senescence, such as *CDKN1A*, *IRF7*, and *ISG15* (**Fig. 1B**). Gene set enrichment analysis
183 (GSEA[51]), using genes expressed above noise level as background, identified several
184 pathways enriched in the PMS iNSCs, including mRNAs encoded by gene sets that drive
185 response to stress (*TNC*, *STAT6*), immune system processes (*THBS1*, *SPP1*), positive
186 regulation of lipid metabolic process (*APOE*, *SREBF1*), regulation of cellular senescence
187 (*CDKN1A*, *IGF1R*), interferon (IFN)-γ signalling (*ICAM1*, *HLA-DPB1*), and transcription factors
188 associated with IFN signalling (*IRF-4*, *IRF-1*, *NF-kB*) (**Fig. 1C, Table S2**). Instead, mRNAs
189 encoded by gene sets associated with cell cycle (*NASP, DPF1*) and telomere organization
190 (*USP7, XRN1*) were al depleted in PMS iNSCs (**Fig. 1D**). This is concordant with previous
191 work identifying cellular senescence in the NSCs of individuals with PMS.[17,24]

192 Next, we investigated the dynamics of gene regulatory networks (GRNs), inferred on
193 differentially expressed genes, associated with enriched terms (inflammation, regulation of
194 cellular senescence, and interferon signalling). We observed a clear hub centred on the
195 senescence gene *CDKN1A*, which then strongly interacted with *CDKN1C*, *CDKN2A*, *STAT1*,
196 and *IRF1* in PMS iNSCs only (**Fig. 1E**). Previous studies have demonstrated that senescence
197 induction via p21 (*CDKN1A*) and p16^{Ink4a} (*CDKN2A*) expression activates IFN response.[52]
198 Density plots of covariation of inflammatory and senescent transcripts (selected based on GO
199 annotations) showed greater difference in weights (i.e. interaction strength/ co-variation in
200 expression) between Ctrl and PMS samples (with stronger covariation in the PMS samples),
201 compared with non-differentially expressed genes (**Fig. S1C**). These results support the
202 predicted interactions between senescence and inflammation pathways.[52] This GRN analysis
203 also supports the hypothesis of an induction of a senescence program only in PMS iNSCs
204 that then promotes IFN and inflammatory signalling activities.

205 Because the sequencing data showed upregulation of genes associated with cellular
206 senescence, we independently validated these findings using Western blot and senescence-
207 associated β-galactosidase (SA-β-gal) staining. We found upregulation of markers of cellular

208 senescence p16^{Ink4a} and GDF15 (**Fig. 1F**)[53] and increased expression of SA-β-gal using
209 SPiDER-β-gal dye in all PMS lines (**Fig. 1G**).[54] Cellular senescence is primarily associated
210 with a halt in cell cycle, which was supported by a depletion of cell-cycle pathways in the
211 mRNAseq (**Fig. 1D**). We then assessed the cycling stage of iNSCs using flow cytometry.
212 Despite iNSCs being analysed under proliferative conditions in chemically-defined media, we
213 still identified a significantly higher proportion of PMS iNSCs in the G1 phase of the cell cycle
214 (*vs* Ctrl), which is typical of quiescent or senescent cells (**Fig. 1H**).[55] Lastly, quantitative
215 (q)PCR-based analysis of relative telomere length revealed that PMS iNSCs have significantly
216 decreased telomere lengths (*vs* Ctrl) (**Fig. 1I**).

217 Therefore, PMS iNSCs phenotypically display intrinsic features of senescence, which are
218 also reflected at the transcriptomic level via upregulation of pathways associated with
219 inflammation and IFN signalling.

220

221 **PMS fibroblasts and iNSCs maintain pathological epigenetic hallmarks**

222 We further investigated the potential origin of the senescent and inflammatory signatures and
223 phenotypes seen in PMS iNSCs. We postulated that the direct conversion from fibroblasts into
224 iNSCs would maintain or even facilitate the emergence of new epigenetic landscapes that
225 further promote the senescence phenotype.

226 To this aim, we assessed the methylation status, genome-wide, using whole genome
227 bisulfite sequencing (WGBS) on the parental fibroblasts and matched iNSC lines. PCA
228 revealed a tight reproducibility of replicates and a clear separation between fibroblasts and
229 iNSCs as well as between Ctrl and PMS samples (**Fig. 2A**).

230 We identified 28 million CpG sites per sample and consistently observed increased
231 hypermethylation in iNSCs (*vs* fibroblasts) (**Fig. S1D-E**). To provide insight to the extent the
232 direct reprogramming reset the aging-related epigenome, we assessed the Cortex Age DNA
233 methylation (DNAm) aging clock using methylation data from the human cortex.[56] The cortex
234 clock predicted an age similar to the chronological age of the donor cells used to generate the
235 iNSCs, suggesting minimal epigenetic resetting occurred during the direct reprogramming
236 (**Fig. 2B**). We also matched this modality against the Horvath and Zhang DNAm clocks, which
237 further confirmed the maintenance of epigenetic age after direct reprogramming for most cell
238 lines (**Fig. S1F**).[57,58] Thus, our own direct reprogramming technology to generate iNSCs from
239 skin-derived fibroblasts maintains epigenetic information from the donor cells.

240 We next investigated methylation commonalities and specific differences between Ctrl and
241 PMS samples in both fibroblasts and iNSCs. We assessed the distribution of differentially
242 methylated regions (DMRs) across genic and intergenic annotations, including a class linking

the DMR to the transcription start sites (TSS) and the resulting distribution was quasi uniform (**Fig. S1G-H**). The differentially methylated cytosines (DMCs) and DMRs indicated an increased hypomethylation in both PMS fibroblasts and iNSCs (*vs* Ctrl; **Fig. 2C, Fig. S1I**). To further explore how these differences in methylation profiles account for transcriptional and phenotypic changes, we investigated genes with hypomethylated DMRs located in proximity of the TSSs. We identified 4,743 genes hypomethylated only in PMS fibroblasts, 3,133 genes hypomethylated only in PMS iNSCs, with 2,344 hypomethylated genes shared between PMS fibroblasts and iNSCs (**Fig. 2D**).

We performed GSEA on the specific hypomethylated genes of the PMS fibroblasts, and found pathways associated with T cell activation, IL-12 production, and JAK-STAT signalling (**Fig. 2E, Table S3**). This was further supported enriched motifs associated with transcription factors in the PMS fibroblasts. These include *SREBP1*, known to regulate T cell growth and survival, as well as *DDIT3*, which is closely connected to JAK-STAT signalling (**Fig. S1J**).[59,60] Gene pathways specific to hypomethylation PMS iNSCs included cytokine production, TNF superfamily cytokine production, and regulation of I-κB kinase/NF-κB signalling (**Fig. 2F**). Additional analyses of enriched motifs identified *STAT5* and *IRF6*, encoding proteins known to be involved in cytokine production, immune response, and senescence (**Fig. S1J**),[61,62] and *ARID5A*, which encodes a protein involved in the immune response by stabilizing *IL-6* mRNA (**Fig. 2F, Fig. S1J**).[63]

To determine which pathways were epigenetically modulated between the PMS fibroblasts and iNSCs, we performed GSEA on genes commonly hypomethylated in both cell types. The results revealed genes encoding proteins with functions in pathways associated with lipid metabolism, inflammation, and IFN production (**Fig. 2G**). In a separate study, we performed metabolomics and lipidomics on the same Ctrl and PMS cell lines, which led to the identification of increased cholesterol synthesis in PMS iNSCs and a new role for this pathway in establishing and sustaining their pathological and neurotoxic phenotype.[46] In addition, using published GWAS studies, genes associated with MS progression and pathology were identified such as leukocyte activation and differentiation, STAT signalling, and IFN production.[64-66] Another example is *IRF5*, known to have associated gene variants in MS,[67] which we found hypomethylated at the promoter-TSS region, in both PMS fibroblasts and iNSCs (**Fig. 2H**).

We also analysed hypermethylated genes, with DMRs located in the promoter regions and in proximity of the TSS. We found 2,946 genes specifically hypermethylated in PMS fibroblasts (*vs* Ctrl), 858 specifically hypermethylated in PMS iNSCs (*vs* Ctrl), and 291 shared hypermethylated genes (PMS fibroblasts *vs* Ctr iNSCs) (**Fig. S1K**). Analysis of the unique differentially hypermethylated genes revealed differences in pathways associated with RNA

279 metabolic processes and cell cycle in fibroblasts and pathways associated with transcription
280 and neuronal differentiation in iNSCs (**Fig. S1L-M**). The hypermethylation pattern of genes
281 that is shared between PMS fibroblasts and iNSCs included DNA-templated transcription and
282 telomerase holoenzyme complex assembly (**Fig. S1N**).

283 To further investigate the epigenetic regulatory modules defined from the WGBS dataset,
284 we used de novo and directed HOMER analysis is to assay for enrichment of shared binding
285 motifs between the PMS fibroblasts and iNSCs. This analysis identified NF-κB*,* a major
286 transcription factor that regulates genes responsible for both the innate and adaptive immune
287 response and is associated with senescence (**Fig. 2I**).[66,68,69] These results were corroborated
288 by the GSEA of the mRNAseq data, where an enrichment in genes associated with NF-κB
289 was also observed in the PMS iNSCs (**Fig. 1C**).

290 Our data suggest that PMS pathology is strongly linked to alterations of the epigenome,
291 which we identified first in patient fibroblasts and confirmed in iNSCs. Many of these epigenetic
292 differences are features of senescence and involve genes that regulate inflammatory,
293 metabolic/lipid, and IFN pathways. Furthermore, when PMS fibroblasts are directly
294 reprogrammed into iNSCs they also adopt an epigenetic landscape that is permissive for
295 increased expression of proteins associated with secretion of inflammatory cytokines,
296 specifically IL-6 and TNF-α.

297

298 **iNSCs share an RG-like signature that is identified in transcriptomic signatures from**
299 **post-mortem human datasets**

300 Next, we explored the heterogeneity of iNSCs and the respective subpopulations driving the
301 phenotypes observed in mRNAseq and WGBSseq sequencing.

302 We first performed single cell (sc) and single-nucleus (sn) RNAseq coupled with ATAC
303 sequencing on the Ctrl and PMS iNSCs to determine if there was a subpopulation of cells that
304 were driving the phenotypes observed in the mRNAseq and WGBSseq (**Fig. S2A**). To
305 minimize technical discrepancies between the two approaches, data-driven, specific filters
306 were applied, on the proportions of reads incident to mitochondrial (MT) DNA and ribosomal
307 proteins (RP). We retained cells with 15-40% RP ratios for the scRNAseq samples and 2-25%
308 RP ratios for the snRNAseq data samples; across the dataset, a 20% MT ratio filter was
309 applied (**Fig. S2B-C**). Additional filters rely on number of UMIs > 8,000, number of genes per
310 cell > 1,000, $\log_{10}$ (genes per UMI) > 0.75. A total of 26,138 cells, across all samples, passed
311 all filtering criteria, with median UMI counts per cell of 22,296. The average number of cells
312 per sample was 3,267, ranging from 1,277 to 5,545; the average number of genes per cell
313 was 5,725, ranging from 4,357 to 6,731 (**Fig. S2D-E**).

314 Using these filtering criteria for RNA analysis, we identified a total of 8 clusters (**Fig. 3A**).
315 We applied the ClustAssess[70] framework to determine the optimal parameters in a data-driven
316 way using the Element Centric Similarity (ECS)[71] as assessment criteria for the crisp
317 partitioning of cells. The type of features (highly variable or most abundant) and number of
318 features retaining signal (i.e. not biased by noise or shallow sequencing) were first determined
319 on 20 iterations of ECS and summarized as element centric consistency (ECC). Next the
320 number of neighbours for the community detection approach and the clustering method was
321 also determined on high ECC distribution. The stable configurations linked number of clusters,
322 number of the most frequent partition, and the resolution parameter (**Fig. S2F-G**). The
323 distribution of ECC across the UMAP indicated a high stability for the selected number of
324 clusters (**Fig. 3B**). We observed a quasi-uniform distribution of cells across all samples and
325 conditions for all clusters (**Fig. S2H**).

326 An indirect assignment of cluster identity was based on co-localisation of expression of
327 standard genes for radial glia (RG), astroglial progenitors, and neuronal progenitors (gene lists
328 in **Table S4**). We found that a majority of the iNSC clusters were defined by an RG-gene or
329 astroglial progenitor gene signature, including the expression of *SOX2*, *NES*, *PAX6*, *PTPRZ1*,
330 *HES1*, and *CKB* mRNAs (**Figs. 3C-D**). The majority of clusters (0-3, 5-7) had a radial glia
331 and/or astroglial progenitor gene signature, encompassing 20-80% of cells within each
332 individual cluster, defined expression thresholds (**Fig. S2I-J**). We also found a small proportion
333 of neural progenitor cells primarily represented by cluster 4 (**Fig. 3E, Fig. S2K**). Genes
334 associated with cell differentiation, including oligodendrocyte progenitor cells (*PDGRA*),
335 oligodendrocytes (*OLIG1*, *OLIG2*, *MBP*), astrocytes (*AQP4*, *ALDH1L1*), and mature neurons
336 (*CALB*, *CCK*) were lowly expressed across the samples and clusters (**Fig. S2L,** gene list in
337 **Table S4**).[72-75] This initial voting-scheme analysis suggests that proliferating iNSCs – similarly
338 to hiPSC-NSCs[76] – are a heterogenous population of cells displaying a transcriptional
339 signature reminiscent of RG-like, astroglial progenitor cells, and a small subpopulation of
340 neural progenitor cells, with little to no detection of terminally differentiated cells.

341 We next assessed the proportion of cells belonging to either Ctrl or PMS iNSCs within the
342 individual clusters. Strikingly, we found mostly equal representation amongst all clusters but
343 cluster 5, which was significantly enriched with PMS iNSCs (**Fig. 3F**). Towards further
344 understanding the biological role of the individual clusters we performed GSEA. Core clusters
345 0, 1, and 3 were enriched for terms linked to CNS development, gliogenesis, and proliferation,
346 while depleted of terms associated with cellular differentiation and pluripotency (**Fig. 3G, Table**
347 **S5**). Cluster 4 was enriched in pathways related to neuronal and cortical development, with a
348 coordinated depletion in the mitotic cell cycle genes (**Fig. 3H**). The remaining clusters were
349 associated with mitochondrial organization and oxidative phosphorylation (cluster 2), glial cell

differentiation (cluster 6), and ion transport (cluster 7) (**Fig. S3A-C**). Cluster 5, showing a striking 6-fold higher frequency in PMS iNSCs (85.6% PMS *vs* 14.4% Ctrl) (**Fig. 3F**), was characterized by genes enriched for cytokine production, immune processes, and IFN signalling, and genes depleted for proliferation and regeneration (**Fig. 3I**).

To evaluate the contribution of cell cycle genes to the transcriptomics signature of clusters, we identified the cell cycle stage using *a priori* defined gene sets. We note a strong representation of cells expressing G1-phase specific genes in cluster 4, a depletion of cells expressing G1-phase specific genes in clusters 1, 2, 3, and a depletion of cells expressing S-phase specific genes in cluster 5, which further supports the GSEA analysis per cluster (**Fig. S3D**).

To investigate the relevance of the *in vitro* iNSC model to human disease, we aligned our *in vitro* results with two independent, publicly available *ex vivo* human snRNAseq datasets from post mortem MS cases and controls.[16,77] Using a panel of canonical RG genes that were also used to characterize the iNSCs (**Table S4**), we identified disease associated RG-like cells within the annotated astrocyte clusters in both datasets (ranging between 6.5 – 7.8% of total astrocyte cluster, **Fig. 3J-K**). When compared to the non-RG-like cells within the astrocyte cluster, RG-like cells exhibited a significantly higher proportion and expression of RG genes *ETNPPL*, *PTPRZ1*, *SOX2*, *PAX6*, and *PCNA* encoding a cell cycle marker (**Fig. S3E-F**). RG-like cells expressed astroglial genes (**Fig. 3C-D**) and very little microglia-specific or oligodendrocyte progenitor cell-specific genes (**Fig. S3E-F**), further supporting their identity. To determine whether these newly identified RG-like cells hold neurogenic potential, we assessed related genes, including *SOX11*, *DCX*, and *TUBB3* and found little expression in both RG-like and non-RG-like cells within the astrocyte cluster in both datasets (**Fig. S3G**). A large proportion of the RG-like cells expressed genes specific of G2M or S phases, which indicated their ability to progress through the cell cycle (**Fig. S3H**). Lastly, we assessed the proportion of RG-like cells across the different MS lesion types. Out of all the RG-like cells in both datasets, we identified that 50% were in chronic active lesions, whereas the smallest proportion of cells were found in control tissue (**Fig. 3L-M**).

Therefore, we identify a small proportion of non-neurogenic RG-like cells in the healthy adult human brain, which significantly increase in frequency in chronic active lesions in the PMS brain.

Patient iNSCs harbour a senescent, IFN-responsive RG-like cell cluster reminiscent of Disease Associated RG the PMS brain

As cluster 5 was predominant in PMS iNSCs (*vs* Ctrl), we sought to further the disease-associated transcriptomic signature of this cluster. Transcriptionally across all samples, cluster

386 5 showed a significant enrichment of genes associated with cellular senescence, IFN α/β
387 signalling, and RIG-I signalling, along with a depletion of genes associated with cell
388 proliferation, DNA-templated transcription, and NOTCH1 signalling (**Fig. 4A**). Cluster 5 also
389 had the highest expression of genes associated with IFN-α and -γ response and the SenMayo
390 gene set[78] (*vs* core clusters 0-3) (**Fig. 4B**). We performed a differential expression analysis
391 followed by GSEA of cluster 5 only specific markers and identified a strong enrichment for IFN
392 and cytokine signalling pathways and SASP that was associated with high expression of *IFIT1*,
393 *ISG15*, and *NLRP2* in PMS iNSCs (*vs* Ctrl) (**Fig. 4C**). We confirmed the high expression of
394 IFN-response genes (*IFIT1*, *IFIT2*) was linked to the hypomethylated promoter regions
395 associated with IFN signalling seen in both PMS fibroblasts and iNSCs, identified in WGBS
396 analysis (**Fig. 2H**).

397 We next wanted to assess the expression of SenMayo and IFN α/β signalling gene sets in
398 RG-like cells from the two human *ex vivo* snRNAseq datasets[16,77] of post-mortem MS brains
399 (**Fig. 4D-E**). A proportion (16-28%) of total RG-like cells – which we termed Disease
400 Associated RG (DARGs) – in chronic lesions showed non-zero expression of the SenMayo
401 gene set, whereas <5% of RG-like cells with the same features were identified in control
402 tissues (**Fig. 4F-G**, **Fig. S4A-B**). We also identified an enrichment in IFN-associated mRNAs
403 in DARGs located in chronic active lesions (**Fig. 4H-I, Fig. S4C-D**).

404 We assessed whether the senescence and IFN-associated expression signatures are
405 unique to DARGs by applying the same expression thresholds to the non-RG-like cells and
406 analysing the datasets. Within chronic active lesions we identified a ~2.3-fold increase in the
407 proportion of senescent DARGs (*vs* senescent non-RG-like cells) in both datasets[16,77] (**Fig.**
408 **S4A-B**). We then compared all lesion areas and identified a ~2-fold increase in the fraction of
409 senescent DARGs in the edge of chronic active lesions, when compared to lesion core,
410 chronic inactive lesion edge, periplaque white matter, and control white matter[16,77] (**Fig. S4A-**
411 **B**). DARGs in *Absinta et al.*[16] showed high expression of IFN-associated genes (*vs* non-RG-
412 like cells) in chronic active lesions (**Fig. S4C**), while displaying the same trend in chronic
413 inactive lesions in *Schirmer et al.*[77] (**Fig. S4D**).

414 These findings provide further support to the existence of non-neurogenic DARGs in the
415 PMS brain, particularly in chronic active lesions, with an inflammatory and senescent
416 transcription signature. Notably, the direct reprogramming of patient somatic cells into stably
417 expandable iNSCs allows for the recapitulation of distinctive disease-associated cellular
418 phenotypes and gene signatures found in the post-mortem MS brain.

419

420 **Disease associated senescent RG-like cells spread dysfunctional features towards**
421 **other clusters**

422 We then performed pseudotime analysis to better understand the developmental trajectories
423 of the RG-like cell cluster of PMS iNSCs with senescent and inflammatory signatures (**Fig. 5**).
424 We removed the neural progenitor-associated cells (cluster 4) which allowed our analysis to
425 focus on the establishment of inflammatory cluster 5. The initialization of the pseudotime
426 focused on cluster 5, defined as the endpoint. The predicted trajectory started with core
427 clusters 0, 1, and 3, progressed to cluster 2 and ended in cluster 5 (**Fig. 5A**). A community-
428 based clustering was applied on the gene expression levels, with the stability assessed using
429 ClustAssess.[70] Several gene modules i.e. clusters of genes with similar expression profiles
430 across the pseudotime were predicted (**Fig. S4E**). We focused on three gene modules with
431 distinct expression patterns. The expression profile of the first module (module 10) focused
432 on the core clusters 0, 1, and 3. A gene enrichment analysis identified significantly elevated
433 expression of genes associated with cell cycle terms, as well as TFs known to maintain
434 NSC/RG identity such as *SP2* (**Fig. 5B, Table S6**).[79] Module 3, which consisted of mostly cells
435 assigned to cluster 2, showed enrichment in terms associated with mitochondria and antigen
436 processing and presentation, including NSC/RG-associated TFs *E2F1* and *PAX6* (**Fig. 5C**).
437 These results support the GSEA enrichment on cluster 2 characterized by mitochondrial and
438 metabolic gene pathways (**Fig. S3B**). Module 7 mostly overlapped with cells in cluster 5 and
439 exhibited enrichment in IFN and cytokine signalling pathways, as well as TFs associated with
440 IFN signalling (*IRF3*, *STAT2*) (**Fig. 5D**). This suggests that the progression towards cluster 5
441 may originate in iNSCs with a cluster 2-like gene signature and display pathways associated
442 with mitochondria and cellular metabolism. Therefore, an altered metabolic signature in PMS
443 iNSCs, which we have recently described,[46] may promote the resurgence of the newly
444 identified IFN responsive RG-like cell cluster 5.

445 Using the modules derived from the *in vitro* dataset, we next identified cells with similar
446 transcriptomic signatures in the *ex vivo* post-mortem datasets.[16,77] Focusing on the
447 recalculated *ex vivo* UMAPs and underlining the RG-like cells (**Fig. 3J-K**), we inferred
448 pseudotime trajectories on both datasets using the core of the RG-like cells (clusters 0, 1, 3)
449 as an initialization point. (**Fig. 5E-F**). Next, we matched the gene modules determined in the
450 *in vitro* and *ex vivo* datasets, respectively. Using the gene lists from the individual modules we
451 cross-referenced the gene modules from the *in vitro* perspective (**Fig. 5B-D**, **Table S6**) and
452 from the *ex vivo* perspective (**Fig. S4F-G**). For the *Absinta et al.* dataset we found coordinated
453 gene expression within modules 5 and 7 that matched our *in vitro* curated modules and module
454 7 matched the inflammatory, senescent cluster 5 (**Fig. 5E, G**) and was associated with DARGs
455 in the chronic active lesion (**Fig. 5G**). In the *Schirmer et al.* dataset we found coordinated gene

456 expression within modules 4 and 7 (**Fig. 5F, H**). Genes that strongly contributed to module 7
457 were associated with chronic inactive lesions (**Fig. 5H**).

458 This analysis highlights the identification of a new cluster of senescent-like, inflammatory
459 non-neurogenic DARGs stemming from astrocyte-like cells in the post-mortem MS brain.

460 As senescence is associated with and perpetuated by secreted proteins, we next
461 investigated ligand-receptor interactions between cluster 5 (as source of ligands) and other
462 clusters (as source of receptors) in iNSCs using NicheNet[80]. With this modelling, Ctrl iNSCs,
463 were enriched for ligand-receptor interactions regulating cell maintenance and differentiation
464 (i.e., Notch signalling) (**Fig. 5I**).[81] However in PMS iNSC, modelling predicted strong
465 interactions between TRAF2 in cluster 5 with TNFRSF1B in clusters 0, 1, and 3, which
466 anticipates induction of NFκB activation[82] and NSC activation,[83] along with a depletion in Wnt
467 signalling via LRP6 (**Fig. 5J-K**).

468 Next, we performed a cluster-by-cluster GSEA analysis and found that clusters 0, 1, and 3
469 in PMS iNSCS were enriched for senescence pathways, particularly those associated with
470 DNA damage and corresponding depleted for proliferation-related terms (**Fig. 5L, Table S7**).
471 We also detected significant interactions between *COL2A1* from cluster 5 and integrin-based
472 receptors in cluster 2 (*ITGB8*, *ITGAV*, *GP6*), coupled with a depletion in NOTCH1 signalling
473 (**Fig. 5J-K**). Enrichment analysis of genes in cluster 2 of PMS iNSCs further indicated
474 enrichment in senescence, IFN signalling, and ECM and corresponding depletion in
475 differentiation and DNA transcription that is known to be regulated by NOTCH signalling (**Fig.**
476 **5L**). Analysis of clusters 4, 6, and 7 consistently identified enrichment of inflammatory-
477 associated terms (i.e., neurodegeneration, oxidative stress-induced senescence, and
478 signalling by Ils) and a depletion in terms associated with NSC maintenance (i.e., Wnt
479 signalling and cell cycle) (**Fig. S4H**). The enrichment in inflammatory terms in PMS iNSCs
480 were linked to increased inflammatory interactions, stemming from cluster 5, between CCR3-
481 CCL5 and between A2M-MMP2 (**Fig. 5J**).

482 To further test the hypothesis that the ligand-receptor interactions predicted above are
483 relevant, we ran a cytokine array on the conditioned media (CM) from the bulk iNSC lines.
484 Quantification of the cytokine array confirmed an increased secretion of cytokines associated
485 with the SASP[84] and inflammation (IL-6, IGFBP-3, and TNFα) in PMS iNSCs (*vs* Ctrl) (**Fig.**
486 **5M**).

487 We then quantified the expression levels of the genes coding for the upregulated SASP
488 (**Fig. 5M**) using our mRNAseq data (**Fig. 1A-E**). Both *TIMP2* and *IGFBP2*, along with the
489 known SASP gene *GDF15*, were upregulated both at gene and protein levels (**Fig. 1F** and
490 **Fig. 5M-N**). Next, we re-analysed the single-cell data for the genes and proteins associated

with the secreted factors identified in the mRNAseq and cytokine array, respectively, and confirmed the elevated expression in cluster 5 of *TNF*, *FN1*, and *ISG15* (**Fig. 5O**).

Overall, our findings suggest that the developmental trajectories of RG-like cells in cluster 5 arise from cluster 2. Additionally, PMS iNSCs secrete inflammatory factors as part of their SASP, and that this may induce a dysfunctional, senescent phenotype in cells in other clusters.

Integrative multi-omics reveals regulons defining inflammatory RG-like cell in PMS iNSCs

To further investigate the epigenetic mechanisms that may contribute to the transcriptomic signature of the PMS iNSC cluster 5, we integrated the RNAseq data with single-nuclei chromatin accessibility data (snATACseq) using both matched and un-matched samples. For a high proportion of cells, the matched RNA and ATAC quantification was distributed proportionally across clusters (**Fig. S5A**). Next, we selected data-driven parameters and stable configuration (high ECC scores) on the ATAC modality using 30 iterations (**Fig S5B-D)** of ClustAssess. We identified 8 stable clusters on the ATACseq dataset.

We then projected the RNA clusters onto the ATAC UMAP, and the ATAC clusters onto the RNA UMAP, respectively to evaluate the concordance of the two modalities (**Fig. 6A-B**). Next, we quantified the equivalence between the RNA and ATAC clusters by summarizing matching cell types/states, which allowed highlighting the agreement between RNA cluster 5 and ATAC cluster 8, well separated in the non-linear space from the other cells (**Fig. 6C**). Then, we confirmed that the inflammatory ATAC cluster 8 was primarily composed of PMS iNSCs (**Fig. S5E**).

We also examined differentially accessible regions (DARs) specific to inflammatory ATAC cluster 8, by selecting the corresponding peaks and enriched motifs on downstream genes, associated with TFs. Our analysis identified that DARs that gained accessibility were associated with immune processes, IFN signalling, and cytokine production (*IRF3*, *STAT2*), and DARs that lost accessibility were associated with genes pertaining to neuron and astrocyte differentiation and neural crest cell fate specification (*SOX4*, *SOX8*) (**Fig. S5F, Table S8**).

We next assessed the overlapping motifs significantly enriched for epigenetic changes in both PMS fibroblasts and iNSCs from the WGBS and from the predicted signature genes of RNA cluster 5, and identified common TFs including *p53*, *E2A*, and *SMAD2* (**Fig. S5G**). As *p53* and *E2A* are implicated in promoting immune function, involved in senescence, and in mediating IFN responses,[85,86] our findings suggest that the chromatin accessibility for RNA cluster 5 closely predicts its RNA expression signature. Biologically, these cells are strongly

526 IFN-responsive and display RG-like signatures. Our identification of common motifs
527 maintained from the fibroblasts during reprogramming to iNSCs in PMS cell types further
528 confirms the involvement of epigenetic regulation in perpetuating the senescent and IFN-
529 response in the iNSCs.

530 Since IFN signalling was found to be strongly involved in RNA cluster 5, we next
531 investigated the chromatin accessibility at the promotor regions. We identified increased
532 accessibility of *IFIT1* in ATAC cluster 8, corresponding to increased expression in RNA cluster
533 5 (**Fig. S5H**). We next investigated genes that are known targets of the regulator of *IFIT1*,
534 *IRF1*, which we identified to be enriched in the bulk mRNAseq of PMS iNSCs (**Fig. 1C**). *IRF1*
535 is a key transcription factor implicated in facilitating TNF-α-induced senescence and is known
536 to be anti-proliferative and pro-inflammatory.[87] Within the IRF1 targets, notably *IFIT3*, *IFIT5*,
537 and *OAS2*, known as IFN-response genes, we found clear associations between RNA
538 expression (RNA cluster 5) and chromatin accessibility near TSS (+/- 3 kb) as well as in
539 potential regulatory regions (+/- 50 kb from TSS) in ATAC cluster 8 (**Fig. 6E**). These data
540 support the hypothesis that cells in RNA cluster 5 have permissive chromatin that underlies
541 persistent activation of IFN-responses via IRF1.

542 The pseudotime analysis predicts RNA cluster 2 was most closely related, and strongly
543 interacting with RNA cluster 5 based on ligand-receptor inference, so we next examined if a
544 similar gene expression and chromatin accessibility signature could be identified in both
545 clusters.

546 Some overlapping genes were found in cluster 2 with similar changes in nearby chromatin
547 accessibility and included inflammatory genes *HAX1* and *SERPINH1* (**Fig. 6E**). Grouped
548 clusters 0, 1, 3 exhibited little expression of *IRF1* target genes. GSEA on shared ATAC
549 signatures, both for gain and loss of accessibility suggested that common gain of accessible
550 regions were associated with stress response and blood brain barrier (BBB) maintenance,
551 whereas loss of accessible sites correlates with notch and BMP signalling, and senescence
552 pertaining to cell proliferation (**Fig. S5I-J**). This downregulation in notch and BMP signalling in
553 cluster 2, based on interactions with cluster 5, was also predicted from the ligand-receptor
554 interaction analysis (**Fig. 5K**). Importantly, not all changes in chromatin accessibility correlate
555 directly to variation in mRNA (**Fig. S5J**).

556 To further understand patterns based on chromatin accessibility and RNA expression, we
557 subdivided gene sets based on RNA upregulation in RNA clusters 0, 1, 3, and depletion in
558 RNA clusters 2 and 5, and found enrichment for terms pertaining to Wnt signalling and NSC
559 maintenance (**Fig. 6F**). We also found increased accessibility near the TSS of the RNA cluster
560 5 upregulated genes, again suggesting aberrant permissive chromatin in these cells promoting
561 increased expression. When assessing coordinated upregulation of gene expression in RNA

562 clusters 2 and 5, we found enrichment in terms associated with mitochondrial transmembrane
563 transport, protein import, and telomerase RNA localization (**Fig. 6F**). These results support a
564 close interaction between RNA clusters 2 and 5, with cluster 5 being specifically IFN-
565 responsive.

566 Lastly, we inferred single-cell regulatory networks using SCENIC[88]. We observed that RNA
567 cluster 5 was defined by two major regulons, *IRF1* and *FOXP2*, that was associated with
568 genes regulating TNF and IFN signalling, as well as the p16-cyclin complex related to
569 senescence (**Fig. 6F, Table S9**). *PAX6* was also identified as a major regulon across all
570 clusters of the iNSCs and was defined by genes associated with nervous system
571 development, supporting their RG-like state. Overall, RNA cluster 5, primarily represented in
572 PMS iNSCs, is consistently defined by gene regulatory patterns that are associated with an
573 IFN-responsive and senescence state.

574 In summary, our work demonstrates that direct reprogramming technology maintains
575 hallmarks of PMS in cells due to maintenance of epigenetic memory. We reveal that patient
576 fibroblasts have hypomethylation at genes associated with lipid metabolic processes and IFN
577 signalling, which then became further accentuated upon direct induction into iNSCs.

578 Within the heterogeneous PMS iNSCs, we identify a novel disease associated cluster of
579 IFN-responsive, inflammatory RG-like cells that display senescent features and are regulated
580 by IRF1, which may spread dysfunctional features towards other clusters through their
581 secreted factors.

582 Integration with publicly available datasets further identifies and highlights a long-neglected
583 non-neurogenic DARG population, which is found significantly increased in chronic active
584 lesions areas and display IFN and senescence gene expression.

585
586
587

588 # DISCUSSION

589 PMS is a complex neuroinflammatory and neurodegenerative disease that results from the
590 interaction between environmental factors and genetic predisposition. The majority of genetic
591 risk factors that have been identified in the development and progression of MS are associated
592 with the peripheral immune system, mapping mainly to T cells, however recent work has also
593 uncovered variants in genes expressed by glial cells.[89,90] MS severity has also been linked to
594 variants involved in mitochondrial function, synaptic plasticity, and cellular senescence in
595 genes expressed in the CNS.[18] To further understand how intrinsic glial cell dysfunction in
596 PMS contributes to disease pathology we generated directly reprogrammed iNSCs.

597 Characterization of directly reprogrammed iNSCs showed PMS donor-derived cells
598 reproduced reported phenotypes of increased expression of inflammatory signalling and
599 senescence associated genes compared to Ctrl cells.[17] Further, patient iNSCs maintained
600 shorter telomere lengths compared to controls, indicating this type of reprogramming better
601 maintains features of the donor cells that may be critical in driving the PMS phenotypes. We
602 then established that iNSCs also maintained epigenetic signatures, as determined by DNA
603 methylation age, after reprogramming from fibroblasts, indicating that this method of cellular
604 reprogramming may conserve epigenetic information important for disease phenotypes.
605 Globally, cell lines derived from people with PMS were found to have lower levels of DNA
606 methylation, with enrichment of hypomethylation at promoter regions of targets for
607 inflammatory transcription factors, such as STAT6 and NFκB. Interestingly, global
608 hypomethylation has been identified to occur with aging in various organs in both mice and
609 humans, which is believed to contribute to genome instability .[91]

610 Concordantly, hypomethylated regions in the PMS fibroblasts and iNSCs were enriched for
611 pathways involved in immune response, suggesting global aberrant epigenetic regulation in
612 individuals with the disease. Previous work has characterized global methylation signatures
613 in the whole blood of people with MS and identified that half of the differentially methylated
614 positions mapped to genes enriched in CNS cells and pathways.[92] This work identified
615 neurodegenerative-related pathways as epigenetically dysregulated in severe MS cases,
616 which correlated with acceleration of methylation age.[92] Intriguingly, we also characterize a
617 loss of methylation in genes that regulate lipid metabolism, implicated in Ionescu, Nicaise et
618 al.[46] Given these pathways appear to be highly relevant to PMS phenotypes, we believe
619 human iNSC methodologies provides an excellent, and biologically valuable, platform for
620 studying mechanisms driving disease.

621 Combined single-cell and single-nucleus RNA data analysis allowed us to better
622 characterize heterogenous iNSCs. Here we identified cells with both neural and RG
623 phenotypes, and importantly were able to find cells with matching transcriptional profiles from
624 datasets generated from post-mortem MS brains. We found that most of the cell clusters were
625 identified by radial glial genes (*SOX2*, *PAX6*), with one cluster which we identified with a neural
626 progenitor signature (*DCX*, *ASCL1*). Within these clusters, we define a novel subset of cells
627 that is predominantly composed of cells derived from PMS donor fibroblasts. This unique RNA
628 cluster 5 displays an inflammatory phenotype expressing many features of senescence and
629 interferon signalling and response.

630 The mechanisms underlying senescence and IFN signalling are intertwined. IFN response
631 can be triggered by a myriad of stimuli, including extra and intracellular double-stranded (ds)
632 RNA and DNA from cell stress and apoptosis, cytosolic DNA, viruses, and microbes, which in

633 turn activates a pro-inflammatory response.[93] Over the course of aging, IFN pathways have
634 been found to become aberrantly activated, which leads to global inflammation (*inflammaging*)
635 and senescence.[94] The presence of an IFN signature in brain cells is increasingly being
636 associated with aging and neurodegenerative diseases in rodent models and humans.[95-98]
637 Type I IFN signatures are found upregulated in the aged brain, especially the choroid plexus,
638 and in neurodegenerative diseases, where it may lead to recruitment and activation of immune
639 cells and eventual neurodegeneration. Interestingly, in our model system, we identify
640 hypomethylation of genes associated with IFN signalling in PMS fibroblasts, indicating a
641 potential predisposition for developing an IFN response in people with PMS. Once fibroblasts
642 are reprogrammed to iNSCs, they take on an even more pronounced IFN phenotype
643 associated with senescence gene expression.

644 From the single-cell data, we establish not only the heterogeneity of iNSCs derived from
645 both Ctrl and PMS donors, but also define a novel subset of disease associated RG-like cells
646 that could be the 'drivers' of the inflammatory signature seen in the analysis of bulk PMS
647 iNSCs. In fact, through ligand/receptor predicted interactions, the secretory factors from this
648 – PMS mostly – IFN-responsive and senescent-like RNA cluster 5, could induce inflammatory-
649 associated signatures (*i.e., neurodegeneration, oxidative stress induced senescence, and*
650 *signalling by Ils*) and inhibit NSC maintenance (*i.e., Wnt signalling, and cell cycle*) in the other
651 iNSC clusters, thus suggesting that RNA cluster 5 can further affect surrounding cells via
652 amplification of such inflammation. Independent work from our group, further supports a key
653 role for disease associated paracrine factors in conditioned iNSC media to induce neurite
654 retraction and neuronal apoptosis.[46]

655 While the mechanisms of this RG-intrinsic intrinsic dysfunctional phenotype in PMS are still
656 unknown, however, we do find epigenetic signatures starting even with the donor fibroblasts.
657 Recently, neurodegenerative diseases have been found to be highly associated with viral
658 exposure,[99] and in the case of MS the Epstein Barr virus (EBV) increases risk of disease.[100]
659 Viral exposure combined with chronic inflammation in PMS may induce global epigenetic
660 changes, affecting cells such as fibroblasts, found to be stressed in people with MS.[101]
661 Furthermore, the activation of human endogenous retroviruses (HERVs) in unique cell
662 populations are also associated with chronic inflammatory neurodegenerative diseases[102] and
663 brain injuries.[103] HERVs can be activated via inflammatory stimuli and induce an IFN response,
664 similar to that of a viral infection.

665 Epigenetically, we identify sites with gains of accessibility are associated with IFN-response
666 and signaling as well as cytokine production in RNA cluster 5 (corresponding to ATAC cluster
667 8) composed mainly of PMS derived cells. The epigenetic remodelling in this cluster was also
668 associated with increased accessibility at binding sites of the p53 motif, known to be activated

669 in response to cellular stress and DNA damage and promotes sustained IFN signaling and
670 response.[85]

671 Using publicly available datasets from MS post-mortem brains, we assessed the
672 expression of RG genes and identified non-neurogenic RG-like cells within well-known
673 astrocyte clusters. Recent work has demonstrated that astrocytes exhibit plasticity in injury
674 situations.[41] Human pathologies which involved lesions and blood-brain barrier rupture were
675 associated with a de-differentiation of astrocytes to replicating NSC/RG-like cells.[41]
676 Furthermore, this has been previously validated in rodent models where epithelial injury allows
677 for neural precursors to dedifferentiate into multipotent NSCs in the olfactory epithelium.[104]
678 Based on these studies, astrocytes in PMS may be undergoing (i) a de-differentiation (or de-
679 maturation) process, where they begin to express cell cycle and early RG-like cell markers
680 due to exposure of chronic inflammation, and a (ii) resurgence as non-neurogenic RG-like
681 cells at the level of disease-associated, ectopic, non-canonical niches.

682 Integration of our *in vitro* iNSC data with publicly available datasets in fact identifies and
683 highlights a long-neglected, non-neurogenic disease-associated RG-like cell population, being
684 found significantly increased in chronic active lesions areas and displaying IFN and
685 senescence gene expression, which we term DARGs.

686 Interestingly, we identify twice as many DARGs in chronic active PMS lesions, which are
687 slowly expanding in nature, feature smouldering inflammatory demyelination at the edge,
688 remyelination failure, and axonal degeneration,[105] and are associated with a more aggressive
689 disease[106]. Further characterization of the phenotype of this novel DARG population showed
690 increased expression of the SenMayo and IFN-associated genes compared to the astrocyte
691 cluster.

692 Overall, our work shows there are epigenetic alterations in somatic fibroblasts isolated from
693 people with PMS, and many of these epigenetic modifications remain following direct
694 reprogramming into iNSCs. These epigenetic alterations are associated with de-repression
695 (hypomethylation and increased chromatin accessibility) of IFN signalling and response as
696 well as inflammation. We further uncover a novel subset of PMS iNSCs with high levels of
697 inflammatory signalling, which we propose drives much of the bulk phenotype.

698 Lastly, we uncover a long-neglected DARG population in the PMS brain, which has similar
699 transcriptomic profiles as the *in vitro* PMS iNSCs, including expression of senescence and
700 IFN transcripts.

701 Our research lays the groundwork for further investigating 'disease-pacemaker' non-
702 neurogenic RG-like cells in potentially driving neuroinflammation in neurodegenerative

disease. Future work is needed to identify the origin and driver of epigenetic dysfunction arising in the cells of people with PMS.

LIMITATIONS OF STUDY

While we generated cell lines from individuals with PMS, the variations in genetic backgrounds, sex, and age among these lines pose a potential limitation. Despite our thorough analysis of both patient and control cell lines, we acknowledge the necessity for additional validation of our findings in situ. Additionally, the inclusion of induced pluripotent stem cells (iPSCs) from the same donors would have enhanced the data quality, allowing for a more robust interrogation of the observed cellular phenomena. Single-cell spatial assays could offer a more comprehensive understanding of our results, particularly in capturing differences related to disease-relevant microenvironments and surrounding cells (neighbours).

ACKNOWLEDGMENTS

The authors wish to acknowledge L. Bonfanti, A. D'Alessandro, V. Fossati, D. Franciotta, C. Frezza, O. Hruba, G. Pluchino, A. Quaegebeur, S. Rizzi, L. Roth and A. Speed for technical and intellectual inputs throughout this study.

This research was supported by the Ferblanc Foundation G112716 (SP and AMN); Catalyst Award from the UK MS Society H160 (SP and CMW); National MS Society Research Grant RG 1802-30200 (SP and LPJ); Bascule Charitable Trust RG98181 (SP); Wings for Life RG 82921 (SP and LPJ), and the Fondazione Italiana Sclerosi Multipla FIMS 2018/R/14 (SP and LPJ) and 2022/R-Single/011 (SP).

BP, DT, JW, LC, JL, JF, SD, MG, and IB are supported by the Intramural Research Program of the National Institute on Aging. AMN is the recipient of a European Committee for Treatment and Research in Multiple Sclerosis (ECTRIMS) Postdoctoral Research Fellowship Exchange Program fellowship (G104956) and is supported through a UK MS Society Centre Excellence grant (G118541). PP is supported through an MRC-DTP and Cambridge Trust PhD studentship and consumable award (RG86932) and Queen's College Tutorial Award. RBI is supported through an MRC-DTP and Cambridge Trust studentship and consumable award (RG86932) and St. Edmund's College Tutorial Award. CW is supported through a National MS Society Post-doctoral fellowship (FG-2008-36954). LPJ was supported by a Fondazione

Italiana Sclerosi Multipla FIMS and Italian Multiple Sclerosis Association AISM Senior research fellowship financed or co financed with the '5 per mille' public funding cod. 2017/B/5 (LPJ), a Wellcome Trust Clinical Research Career Development Fellowship (G105713), and a National MS Society Research Grant RFA-2203-39318. FE was supported by the Austrian Science Fund FWF (FWF-INTER – INTER/FWF/19/14117540/Pdage and the SFB F78 "Neuro Stem Modulation", SFB F7810-B). LP and IM are supported by Wellcome Trust (203151/Z/16/Z) and the UKRI Medical Research Council (MC_PC_17230).

AUTHOR CONTRIBUTIONS

Conceptualization, BP, AMN, DT, IM, SP, IB; Methodology, BP, AMN, DT, JW, LC, JL, RBI, JF, SD, MSC, AS, TL; Investigation, BP, AMN, DT, LP, PP, MLDN, LC, JL, RBI, CMW, GK, TL, MG, IM, SP, IB; Writing – Original Draft, BP, AMN, DT, LP, IM; Writing – Review & Editing, AMN, DT, IM, SP, IB; Funding Acquisition, AMN, CMW, LPJ, IM, SP, IB; Resources, JF, SD, MSC, AS, TL, FE; Supervision, MG, IM, SP, IB.

DECLARATION OF INTERESTS

SP is founder, CSO and shareholder (>5%) of CITC Ltd and Chair of the Scientific Advisory Board at ReNeuron plc. The other authors declare that they have no competing interests.

FIGURE LEGENDS

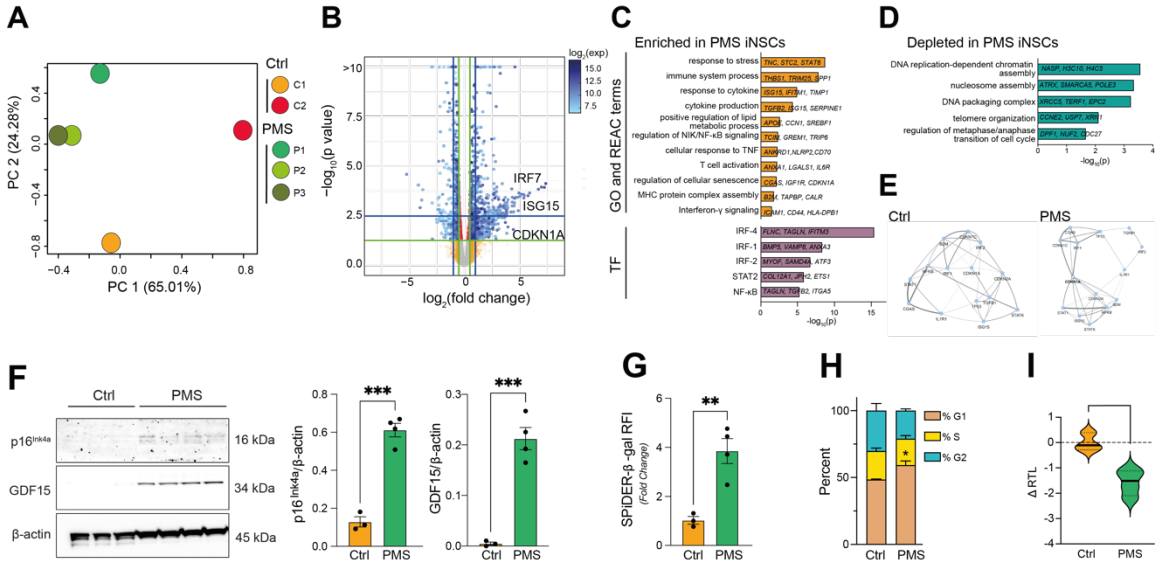

Figure 1. Bulk mRNAseq reveals increased inflammatory signalling and senescence markers in PMS iNSCs.

A) PCA summarizing the co-variation of expression levels in the mRNA sequencing. C and P are independent cell lines (**Table S1**).

(**B**) Volcano plot illustrating differentially expressed genes, *vs* $\log_2$ abundance in PMS iNSCs compared to Ctrl iNSCs. Log_2(FC) *vs* adjusted p-values (with Benjamini Hochberg multiple testing correction) are reported.

(**C-D**) Pathway enrichment analysis on GO and REAC terms and enriched transcription factors (TF) based on TransfFac annotation, from mRNA sequencing.

(**E**) Gene regulatory networks, inferred on manually curated, differentially expressed genes contrasting of Ctrl *vs* PMS iNSCs networks, derived from the mRNA sequencing.

(**F**) Representative western blots and quantification for $p16^{Ink4a}$, GDF15, and β-actin.

(**G**) Quantification of relative fluorescence intensity (RFI) of senescence-associated β-galactosidase expression using SPiDER-β-gal. Data represented as a fold change over Ctrl iNSCs.

(**H**) Flow cytometry-based quantification of iNSC cell cycle states. Data plotted as cells in percent of cell cycle state.

(**I**) Quantification of changes in PMS relative telomere length (RTL) over Ctrl iNSCs.

Experiments in **F-I** were done on n= 3 Ctrl and n= 4 PMS iNSC lines each performed in n= 3 replicates. Data in **F-I** are mean values ± SEM. *$p \leq 0.05$, **$p \leq 0.01$, ***$p \leq 0.001$, un-paired t-test, with unequal variances.

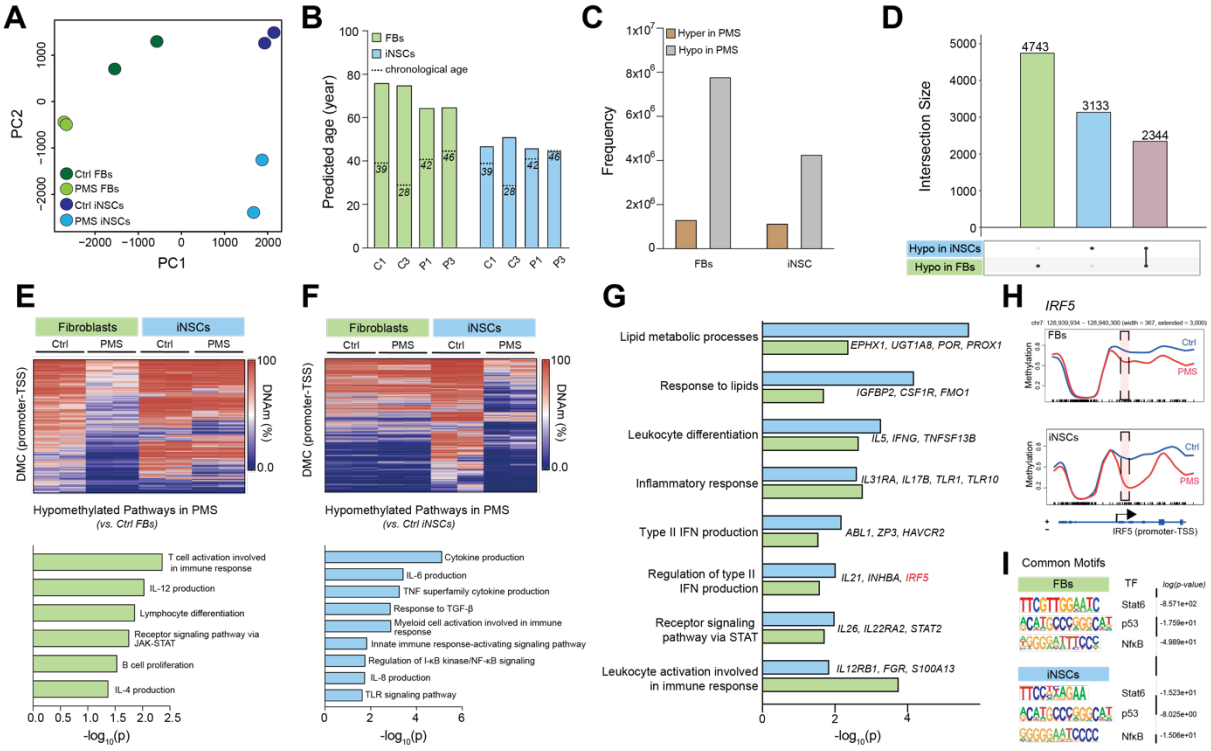

Figure 2. Whole genome bisulfite sequencing (WGBS) uncovers inflammatory pathways found commonly hypomethylated in PMS fibroblasts and iNSCs.

(**A**) PCA summarizing methylation quantified in the WGBS data for fibroblasts and iNSC samples (**Table S1**).

(**B**) Cortex age DNA methylation aging clock inference. Dashed line indicates chronological age at which FBs samples were sampled.

(**C**) Frequency of differentially methylated cytosines (DMC), plotted as Ctrl *vs.* PMS.

(**D**) UpSet plot of hypomethylated genes within the promoter-transcription start site (TSS) region.

(**E-F**) Heatmap and enrichment analysis of hypomethylated genes.

(**G**) Enrichment analysis of commonly hypomethylated genes in PMS (*vs* Ctrl) fibroblasts (light green) and iNSCs (light blue).

(**H**) Example of methylation difference for *IRF5* (genome browser tracks), as in **G**.

(**I**) Proportional sequence logos on HOMER motifs resulting from an enrichment analysis from **E**.

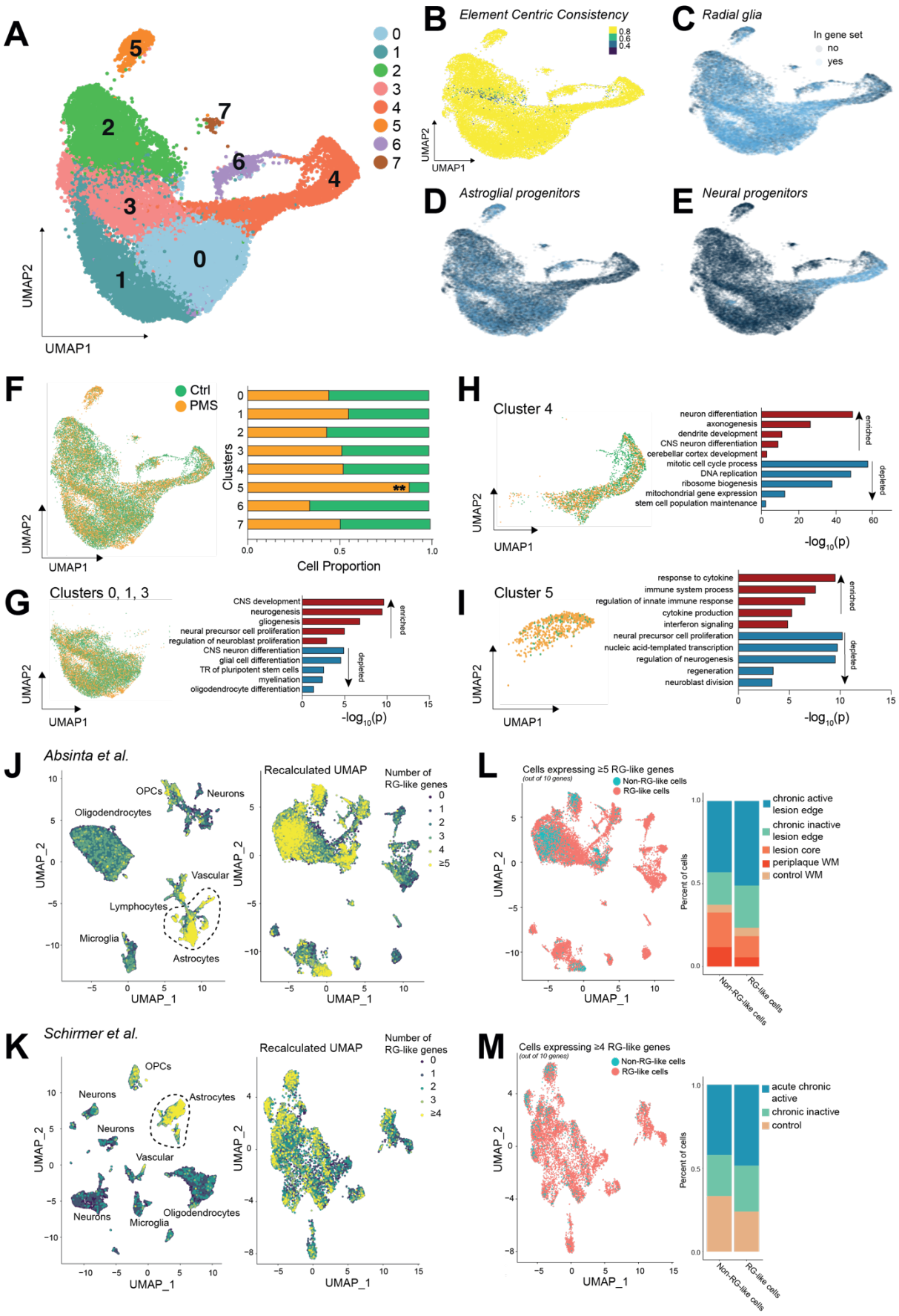
A
B Element Centric Consistency
C Radial glia
In gene set
no
yes
D Astroglial progenitors
E Neural progenitors
UMAP1
UMAP2
F
Ctrl
PMS
Clusters
Cell Proportion
H
Cluster 4
neuron differentiation
axonogenesis
dendrite development
CNS neuron differentiation
cerebellar cortex development
mitotic cell cycle process
DNA replication
ribosome biogenesis
mitochondrial gene expression
stem cell population maintenance
enriched
depleted
-log10(p)
G
Clusters 0, 1, 3
CNS development
neurogenesis
gliogenesis
neural precursor cell proliferation
regulation of neuroblast proliferation
CNS neuron differentiation
glial cell differentiation
TR of pluripotent stem cells
myelination
oligodendrocyte differentiation
I
Cluster 5
response to cytokine
immune system process
regulation of innate immune response
cytokine production
interferon signaling
neural precursor cell proliferation
nucleic acid-templated transcription
regulation of neurogenesis
regeneration
neuroblast division
J
Absinta et al.
OPCs
Neurons
Oligodendrocytes
Vascular
Lymphocytes
Microglia
Astrocytes
UMAP_1
UMAP_2
Recalculated UMAP
Number of RG-like genes
L
Cells expressing ≥5 RG-like genes
(out of 10 genes)
Non-RG-like cells
RG-like cells
Percent of cells
chronic active lesion edge
chronic inactive lesion edge
lesion core
periplaque WM
control WM
K
Schirmer et al.
Oligodendrocytes
M
Cells expressing ≥4 RG-like genes
acute chronic active
chronic inactive
control

801

802 **Figure 3. iNSCs display a RG-like transcriptomic signature that can be identified in the**
803 **adult human brain using single nuclei sequencing.**
804 (**A**) UMAP of Ctrl and PMS iNSC single-cell, -nucleus RNAseq samples, post quality checking
805 and filtering; a stable partitioning of cells is also highlighted.
806 (**B**) Element centric consistency, derived on 30 iterations, calculated per cell, and visualized
807 on the RNA UMAP.
808 (**C-E**) Voting scheme of genes associated with a RG-like signature (**C**), astroglial progenitor
809 signature (**D**), and neural progenitor signature (**E**) as in **A**.
810 (**F**) Cluster distribution in human iNSCs on the RNA UMAP. The histogram summarizes cell
811 proportions per cluster. $^{**}p \leq 1e\text{-}106$ (X^2 test).
812 (**G-I**) Enrichment analysis of enriched and depleted terms in clusters 0, 1, 3 (**G**); cluster 4 (**H**);
813 cluster 5 (**I**) *vs* all other clusters; recalculated RNA UMAPs illustrating the distribution Ctrl *vs*
814 PMS cells.
815 (**J-K**) Recalculated UMAPs of RG-like cells in two *ex vivo* MS datasets, *Absinta et al., 2021*
816 (**J**) and *Schirmer et al., 2019* (**K**). OPCs, oligodendrocyte progenitor cells.
817 (**L-M**) Voting scheme UMAPs and histograms summarizing the frequency of RG-like cells (and
818 non-RG-like cells per area of interest as in **J-K**. WM, white matter.
819

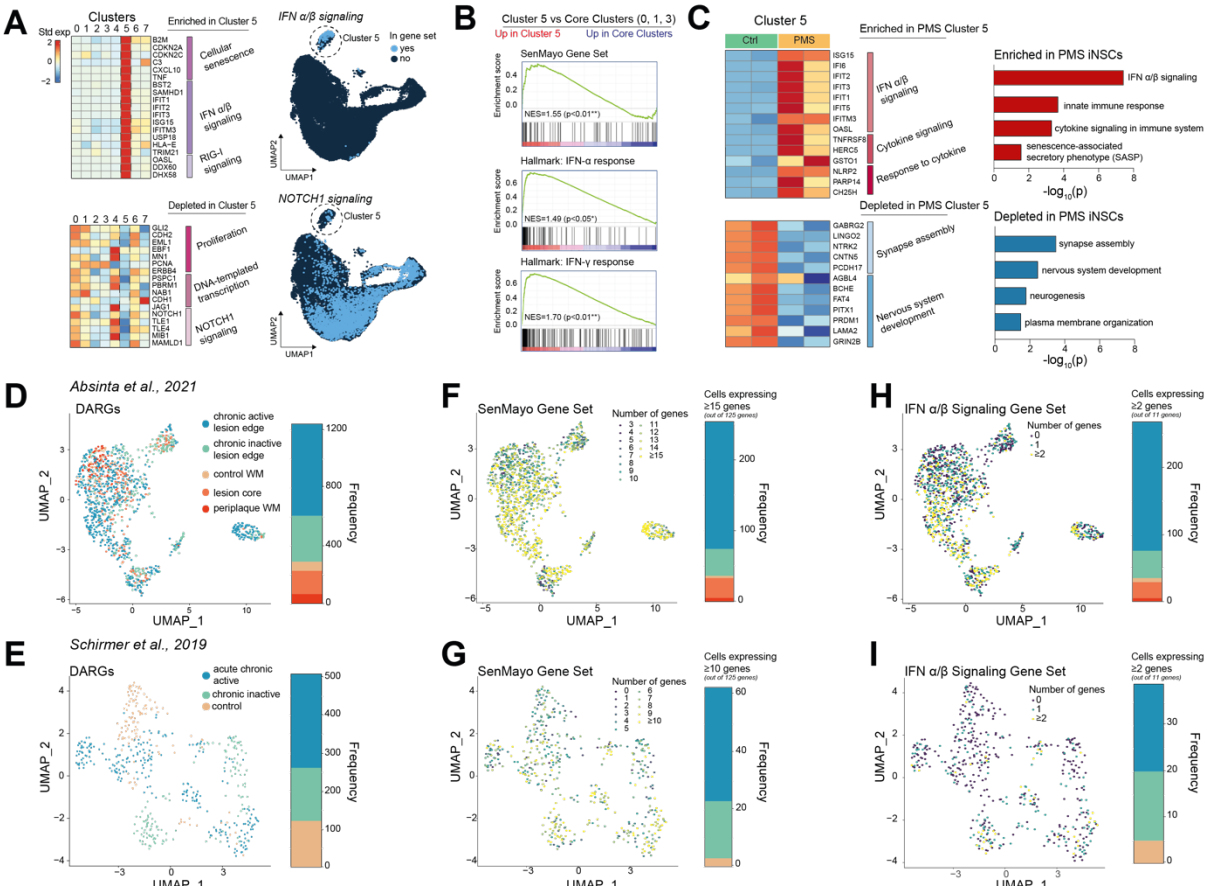

Figure 4. A specific PMS iNSC cluster displays senescence and IFN-signalling which is also identified in DARGs of the PMS brain.

(**A**) Heatmap of RNA cluster 5 signature markers and summary of associated enrichment terms. Voting scheme UMAP of genes associated with IFN- α/β signalling and NOTCH1 signalling.

(**B**) Enrichment plots of the SenMayo gene set, and the IFN-α, and IFN- γ response in cluster 5.

(**C**) Heatmap of standardized expression of highly expressed *vs* depleted transcripts, specific to only PMS cells *vs* Ctrl cells in RNA cluster 5 and selected enriched pathways significant for the selected genes.

(**D-E**) Recalculated UMAP on the filtered cells identified as DARGs in **Figure 3L-M**. Stacked Histograms summarizing the frequency of cells per lesion area.

(**F-I**) UMAPs and histograms of DARG frequency that express genes in the SenMayo gene set and IFN- α/β signalling gene set respectively from *Absinta et al., 2021* and *Schirmer et al., 2019* data.

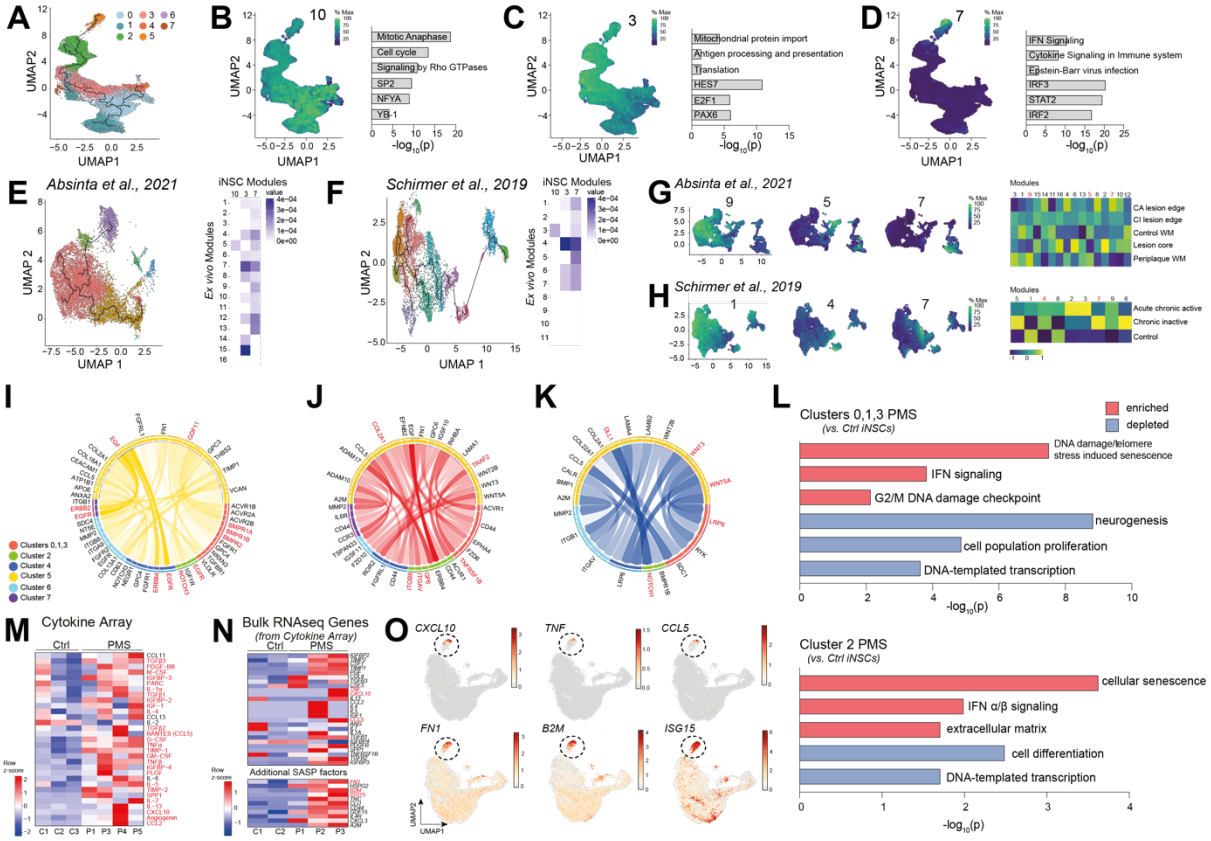

Figure 5. PMS iNSCs secrete a pro-inflammatory SASP that induces upregulation of genes associated with inflammation and senescence.

(**A**) Pseudotime trajectory inferred and displayed on the *in vitro* dataset UMAP. Cluster 5 was used as initialization point (*endpoint*).

(**B-D**) UMAP of the distribution of intensity of genes clustered in modules 10 (**B**), 3 (**C**), and 7 (**D**), determined based on the pseudotime ordering. GSEA summary and TFs corresponding to gene modules 10 (**B**), 3 (**C**), and 7 (**D**).

(**E-F**) UMAP of pseudotime trajectory inferred from the *Absinta et al., 2021* (**E**) and *Schirmer et al., 2021* (**F**) datasets, respectively. The heatmaps summarize the scaled proportions of common genes matching between iNSC *in vitro* modules 10, 3, and 7 with *ex vivo* modules.

(**G-H**) Modules selected from the *ex vivo* datasets as in **E-F** recapitulating the manually curated modules (**B-D**) identified on the *in vitro* pseudotime trajectory. The heatmaps summarize the scaled averaged expression of the *in vitro* gene modules, projected on the *ex vivo* datasets.

(**I-K**) Circos plots of the intercellular ligand-receptor interactions predicted using NicheNet. (**I**) Yellow directed edges indicate interactions, (**J**) red edges summarize enriched ligand/receptor interactions i.e. upregulated target genes, (**K**) blue edges summarize depleted ligand/receptor interactions i.e. downregulated target genes, between cluster 5 and complement clusters in Ctrl and PMS iNSCs.

(**L**) Enrichment summary on enriched and depleted genes in clusters 0,1,3 and cluster 2 (Ctrl *vs* PMS).

(**M**) Heatmap of cytokine array performed on CM. Colour intensities are proportional with standardized normalized intensities. Proteins investigated also in the mRNAseq (**N**) are highlighted in red.

(**N**) Heatmap of standardized normalized expression levels of genes coding for secreted proteins as in **M**. Genes investigated also in the single cell data (**O**) are highlighted in red.

(**O**) Expression gradient UMAPs of the selected secreted proteins as genes (**N**).

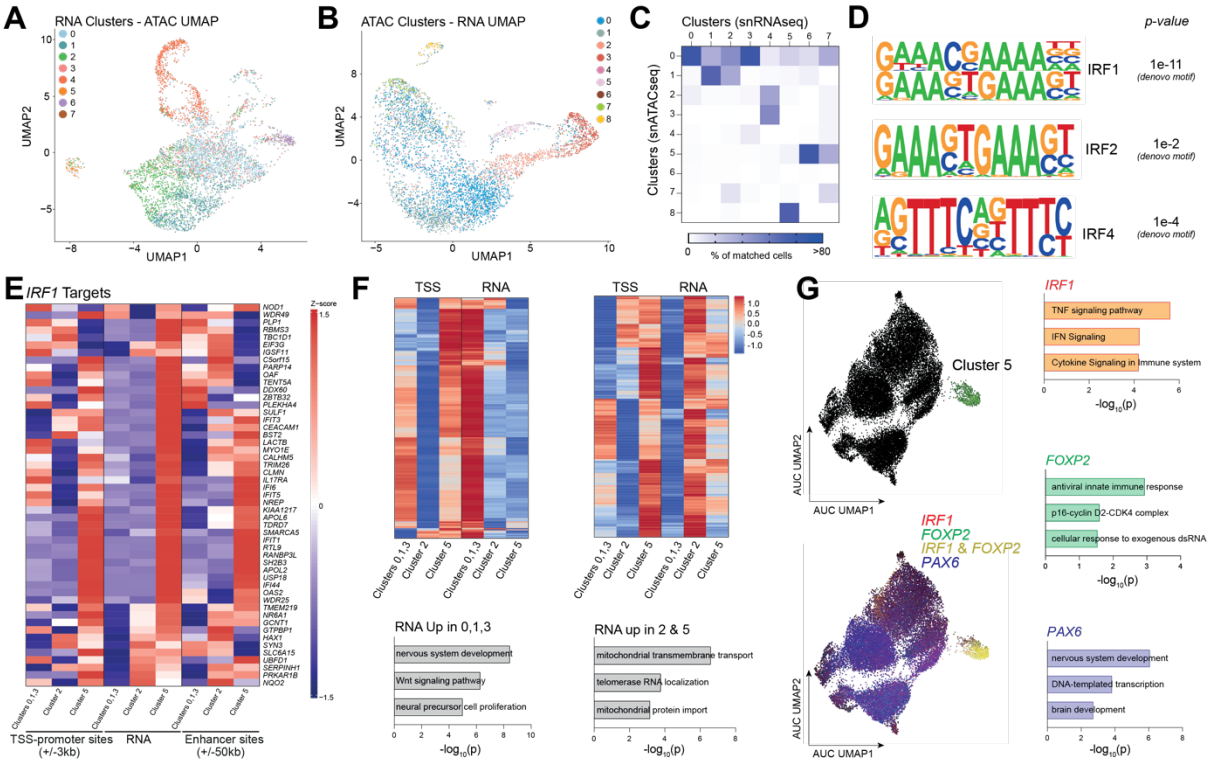

Figure 6. Multi-omics RNA/ATAC integration with further epigenetic characterization of cluster 5 cells.

(**A**) ATAC UMAP of the overlaid localization of RNAseq clusters.

(**B**) RNA UMAP of the overlaid localization of snATACseq clusters.

(**C**) Heatmap of the percentage of matched assignations of cells across the snRNAseq and snATACseq clusters. The analysis was performed solely on matched cells i.e. cells with both RNA and ATAC expression.

(**D**) Enriched motifs of signature and differentially accessible genes identified on the RNA cluster 5, and ATAC cluster 8.

(**E**) Heatmap of accessibility (ATAC) and expression (RNA) of *IRF1* targets, i.e. TSS, RNA, and distal portions of marker genes identified as differentially expressed between grouped RNA clusters 0, 1, 3 *vs* cluster 2, and cluster 5, respectively.

(**F**) Heatmap of marker genes, between clusters 0, 1, 3 *vs* 2 and 5. The summary of enrichment analysis applied on the selected genes.

(**G**) SCENIC GRN inference summary and selection of IRF1 specific regulons, corroborated with enrichment analysis of regulons (*IRF1*, *FOXP2*, *PAX6*). The GRN inference was performed on the scRNAseq dataset.

METHODS

Data and code availability

All codes used in the study are available on github: https://github.com/Core-Bioinformatics/DARG_PMS

- Any additional information required to reanalyse the data reported in this paper is available from the lead contacts upon request.
- All data generated for this study, in raw and processed format, are publicly available on the Gene Expression Omnibus (GEO), under accessions GSE243319, GSE251839, GSE251831, GSE251838, and GSE251830. Further data mining of processed data may be performed on bulkAnalyseR for bulk sequencing datasets and ClustAssess and Shiny Cell apps (https://bioinf.stemcells.cam.ac.uk/shiny/pluchino/DARG_PMS/bulkanalyser/, https://genomicspark.shinyapps.io/shinyApp/) for single-cell/ nuclei datasets. UCSC genome browser sessions for these datasets comprise: https://genome-euro.ucsc.edu/s/CSCI/DARG_PMS and http://tinyurl.com/2ygsa6or.

EXPERIMENTAL MODEL AND SUBJECT DETAILS

Patient cells

The cohort consists of 5 PMS and 3 healthy controls between 25 and 63 years of age. The cohort includes representation from both genders, distributed across PMS and control groups (Table S1). PMS fibroblasts were provided by the New York Stem Cell Foundation (NYSCF) Research Institute through their Repository (http://www.nyscf.org/repository)[107]. Patients were recruited at the Tisch Multiple Sclerosis Research Center of New York, upon informed consent and institutional review board approval (BRANY). PMS donors underwent clinical assessment when recruited for the study. Control fibroblasts C1 and C2 (Table S1) were generated from adult dermal fibroblasts after obtaining consent and ethical clearance by the ethics committee of the University of Würzburg, Germany.

Generation and culturing of induced neural stem cells

iNSC lines were generated and quality controlled as described in *Ionescu, Nicaise et al.*[46] and *Meyer et al.*[45] iNSCs were maintained in neural induction media (NIM) consisting of DMEM/F12 and Neurobasal (1:1) (ThermoFisher), supplemented with N2 supplement (1x) (ThermoFisher), 1% glutamax (ThermoFisher), B27 supplement (1x) (ThermoFisher), CHIR99021 (3 μM) (Cell Guidance Systems), SB-431542 (2 μM) (Cayman Chemical), and hLIF (10 ng/ml) (PeproTech) until 70% confluent, then lifted using accutase, spun at 300 x g for 3 mins, and plated onto growth factor reduced (GFR) matrigel matrix coated plates

920 (Corning) (1:20 in DMEM/F12) with Y-27632 (10 μM) (Miltenyi Biotec) between 1:3-1:5 in NIM
921 media. Media was changed every second day as needed. Experiments were performed on
922 cells from passages 20-35.
923
924 **Fibroblast maintenance**
925 Fibroblasts were maintained in growth medium (DMEM Glutamax I [Thermo Fisher])
926 supplemented with 10% fetal bovine serum, 1% non-essential amino acids and 1 mM sodium
927 pyruvate (ThermoFisher) at 37°C with 5% CO_2 and fed every 3-4 days. After reaching 90%
928 confluency the fibroblasts were detached with trypsin-EDTA 0.05% for 5 min followed by
929 neutralization in DMEM and spun down at 300xg for 5 min. They were split 1:4 into growth
930 media onto tissue-culture treated plasticware.
931
932
933 **METHOD DETAILS**
934 **mRNA sequencing, analysis, and inference of Gene Regulatory Networks (GRNs)**
935 iNSC lines, between passages 15-30, were plated at 500,000 cells per well in GFR-coated 6-
936 well plates. After 24 hours, the media was refreshed with new NIM. Cells were harvested in
937 RLT lysis buffer 72 hours after plating then frozen at -80°C until extraction. RNA extraction
938 was performed according to standard steps described for the RNeasy kit, followed by DNase
939 treatment (Qiagen). RNA was quantified using the NanoDrop 2000c instrument. Illumina
940 Sequencing libraries were prepared using the TruSeq low sample protocol from 1 μg of total
941 RNA (Illumina, San Diego, CA, USA). The resulting libraries were sequenced in paired-end
942 mode, on 150 nts reads on an Illumina NovaSeq 6000 instrument.
943 The quality checking of the samples was assessed using fastQC v0.12.11, applied on raw
944 files; the outputs were summarised using multiQC 1.14.[108] Initial sequencing depths ranged
945 from 30M to 44M reads; subsampling without replacement, done using seqtk 1.3-r106 [109], was
946 performed to 34M reads, to avoid inconsistencies caused by uneven sequencing depths.[110]
947 All samples were aligned to the GRCh38.p13 genome using STAR 2.7.10a (paired-end
948 mode).[111] Expression quantification was performed using featureCounts v.1.6.3.[112] The
949 distribution of signal across transcripts was assessed on the UCSC genome browser. The
950 tracks (bigwig format) were built from the bam files using samtools 1.17.[113] Next, noisyR 1.0.0[48]
951 was used to estimate and remove noise from the count matrix; the raw expression levels were
952 normalised using quantile normalisation.[114] Differentially expressed genes (DEGs) were
953 identified using edgeR[50] and DESeq2[49]; due to the noise correction the DEG calling
954 converged; p-values were adjusted using Benjamini-Hochberg multiple testing correction.

955 bulkAnalyseR 1.1.0[47] was used to build a shareable interface for the analysis and visualisation
956 of data.
957 The Gene Regulatory Networks (GRNs) were predicted, and their dynamics assessed, on the
958 bulk RNAseq data using a bulkAnalyseR ShinyApp.[47] Additional analyses were performed
959 using GENIE3[115] and visNetwork[116] to visualise subgraphs according to selected pathways
960 and a maximum of 30 edges. To assess the global trend in co-variation of expression, for
961 genes annotated to the selected pathways, density plots were created, per pathway, on the
962 weights of the edges in the larger GRNs (corresponding values in the global adjacency matrix).
963
964 **Immunoblotting**
965 iNSCs were homogenized in 10X RIPA buffer (Abcam) supplemented with 100X protease and
966 phosphatase inhibitors (ThermoFisher). Protein concentration was assessed using a BCA
967 assay (ThermoFisher). Equal protein amounts (25 µg) were resolved by SDS-PAGE on Bolt™
968 Bis-Tris Plus pre-cast 4-12% gradient gels (Invitrogen) and transferred to 0.45 mM
969 polyvinylidene fluoride (PVDF) membranes (Thermo Scientific). Membranes were blocked
970 with TBS blocking buffer (LI-COR Biosciences) and immunoblotted with the indicated
971 antibodies: mouse anti-p16^{Ink4a} (Invitrogen) at 1:500, rabbit anti-GDF15 (Proteintech) at
972 1:1000, and mouse anti-b-actin (Sigma) at 1:5000 in TBS blocking buffer (LI-COR
973 Biosciences) with 0.1% Tween, followed by fluorescent secondary antibodies IRDye 680RD
974 Goat anti-Rabbit or IRDye 800CW Goat anti-Mouse (LI-COR Biosciences) at 1:10,000 in TBS
975 blocking buffer (LI-COR Biosciences) with 0.1% Tween and 0.01% SDS. The immunoblots
976 were visualized with the ChemiDoc MP Imaging system (Bio-Rad). Densitometric analysis was
977 conducted with Fiji by ImageJ. Protein targets were normalized to β-actin.
978
979 **SPiDER-gal**
980 Cells were plated on black-walled, clear bottom 96-well plates (ThermoFisher, 165305) at
981 15,000 cells/well and maintained in culture for 5 days. Expression of senescence associated
982 β-galactosidase was measured by a SPiDER- β-gal-based cellular senescence plate assay kit
983 (Dojindo) according to manufacturer's instructions. Briefly, cells were washed with PBS,
984 stained with 1 µg/mL Hoechst (Sigma-Aldrich) as a measure of cell number, washed again,
985 before the fluorescence intensity was measured at 358nmEx/461nmEm. Cells were then lysed
986 with the provided buffer and the SPiDER-β-gal stain was added and incubated at 37°C
987 overnight. Fluorescence intensity was measured at 520ex/565em. The SPiDER-β-gal
988 fluorescence intensity of each well was corrected for the autofluorescence of empty wells and
989 normalized to the Hoechst fluorescence intensity of the respective well to normalize for cell

990 number. The resulting average SPiDER-β-gal/Hoechst fluorescence intensity of each cell line
991 was normalized to that of healthy control cell lines.
992
993 **Cell Cycle Analysis**
994 iNSCs were plated at a density of 80,000 cells/cm^2 on GFR-coated plates. After 3 days cells
995 were lifted using accutase and then pelleted at 500 x g for 5 minutes. The cells were fixed in
996 70% ethanol for 30 minutes on ice then pelleted at 850 x g for 5 minutes. The cell pellet was
997 resuspended in RNase (100 ug/mL) for 15 minutes and incubated at room temperature.
998 Propidium iodide (1 ug/mL) was added to each sample and cells were analysed on a BD
999 LSRFortessa with the flow rate on slow. 20,000 events were collected for each sample. The
1000 data was analysed using FlowJo 10.9 software using the Dean-Jett-Fox approach.
1001
1002 **Telomere length analysis**
1003 Relative telomere length was assessed using the *Joglekar et al*. protocol using quantitative
1004 PCR (qPCR) and comparison to that of a single copy gene.[117] iNSCs were plated at a density
1005 of 80,000 cells/cm^2 on GFR-coated plates. After 3 days cells were lifted using accutase and
1006 then pelleted at 500 x g for 5 minutes. DNA was isolated according to the DNeasy Blood &
1007 Tissue Kit (Qiagen) and quantified using the Nanodrop 2000c instrument. For initial
1008 optimization of the qPCR reaction, the DNA was diluted to three different concentrations (100
1009 ng/μL, 25 ng/μL, 6.25 ng/μL), and it was determined that 100 ng/uL had the best efficiency for
1010 both the human β-globulin and telomere primers. Two PCR reactions were separately
1011 conducted, for human β-globulin the mastermix was made using 5 μL Fast SYBR Green
1012 (ThermoFisher), 1 μL of hbg1 primer (3 μM), 1 μL of hbg2 primer (7 μM), and 2 μL of nuclease-
1013 free water. The reaction was cycled at 58°C annealing temperature along with a melt curve
1014 analysis using a QuantStudio 7 Flex (ThermoFisher). For the telomere primers, the mastermix
1015 was made using 5 μL Fast SYBR Green (ThermoFisher), 1 μL of telomere A primer (1 μM), 1
1016 μL of telomere B primer (3 μM), and 2 μL of nuclease-free water. The reaction was cycled at
1017 56°C annealing temperature along with a melt curve analysis using a QuantStudio 7 Flex
1018 (ThermoFisher). Each sample was run in duplicate. Average telomere length was calculated
1019 as the ΔΔCT = (PMS average hbg Ct – PMS average telomere Ct) – (Control hbg Ct – control
1020 average telomere Ct).
1021
1022 **Whole genome bisulfite sequencing (WGBS)**
1023 Genomic DNA was extracted from 100,000 fibroblasts and iNSCs using the DNeasy Blood
1024 and Tissue Kit (Qiagen). The quantity of DNA was measured using the Quant-iT PicoGreen
1025 method and victor X2 fluorometry (ThermoFisher), and the integrity of the DNA was evaluated
1026 with Agilent genomic DNA screen tape. 500 ng of genomic DNA was used for sequencing. The

1027 sample quality control criteria for the WGBS library were set to having a DNA integrity number
1028 (DIN) score of 7.0 and above. The extracted DNA was fragmented to an average insertion
1029 size of 550 base-pairs and the fragments were attached to end-repaired adapters. Genomic
1030 DNA was bisulfite converted using the EZ DNA methylation Gold kit (Zymo, Catalog #D5005)
1031 following the manufacturer's instructions. We next applied the xGen Methyl-Seq Lib Prep kit
1032 (Integrated DNA technologies, Catalog #10009824) to the prepare the genomic DNA library.
1033 Library quality control was performed using qPCR (LightCycler 480) and TapeStation 4200
1034 (D1000 screen tape).
1035 The dataset comprises 8 samples (4 fibroblast lines and 4 iNSC lines), with sequencing depths
1036 varying from 213M to 408M, and an average of 315M reads per sample. Reads with adapter
1037 contamination were trimmed using Trim Galore (0.4.3)[118] with options: --paired –q 25. Trimmed
1038 reads were aligned to the *H sapiens* reference genome (version hg38), using HISAT2[119]
1039 (version built in the current stable version of Bismark 0.23.1[120]). A bisulfite-converted index
1040 (GA and CT conversion) was generated with default parameters. We identified 28M CpG sites
1041 per sample, with sequencing coverage varying from 24x to 39x, (an average of 30x coverage
1042 per sample). The bismark_methylation_extractor tool was used to summarize the methylation
1043 levels at CpG sites. After assessing the bias at 5'end regions using M-bias results, the first
1044 2nts were excluded, as follows: bismark_methylation_extractor -p –ignore 2 –ignore_r2 –
1045 comprehensive –no overlap –bedGraph –counts –buffer_size 16G ($Aligned read bam file).
1046
1047 **Identification of differentially methylated sites and regions**
1048 MethylKit[121] was used for DMC and DMR quantifications, and fibroblast *vs* iNSC comparisons.
1049 A minimum threshold minimum of 10nts coverage for downstream DNA methylation analysis
1050 was set. The aligned reads were split into 100nt tiles (DMRs) using metilene.[122] Differential
1051 methylation was calculated, applying a McCullagh and Nelder[123] correction for overdispersion,
1052 as well as the sliding linear model (SLIM) proposed in methylKit to correct for multiple testing.
1053 Tiles with a q-value < 0.05 and over 20% methylation difference were called differentially
1054 methylated. Motif enrichment analysis was performed using Homer (*findMotifsGenome.pl*).
1055 Annotations relevant for the hg38 v6.4 of the *H sapiens* reference genome (genes, exons,
1056 introns, UTRs, and other annotations) were extracted using Homer annotation tools.
1057 AnnotatePeaks.pl DMR hg38[124] was used to evaluate the distribution of methylation across
1058 the genome. Next, a comparative analysis of the DMRs/DMCs across tissue types, contrasting
1059 the control and PMS samples was performed. In addition to the number of methylated tiles
1060 per annotation category was calculated, as well as their distance to the closest Transcription
1061 Start Site (TSS). To calculate the epigenetic age, we applied the Shireby-Cortex,[56] Hovarth,[57]
1062 and Zhang,[58] ageing clocks frameworks. For the Hovarth and Zhang estimations Clockbase
1063 platform[125] was used, relying on matched Illumina methyl array IDs. The DNA methylation

levels (0-100%) per CpG probe, and the sample metadata were submitted to Clockbase, and the predicted clock age was downloaded as CSV format. For the Shireby-Cortex[56] aging estimate, we downloaded the DNA methylation probes, and coefficient values and relied on matched Illumina methyl array IDs. We used total 347 DNA methylation CpG probes to predict epigenetic aging (> 20nts coverage).

Nuclei isolation, library preparation, and RNA sequencing

For the single-nucleus single-omics, (ATAC) and multiomics experiments, respectively, 2 x10^6 cells were harvested; nuclei were isolated following the manufacturer's instructions with minor modifications. Briefly, cells were lysed in 100 µL of freshly prepared lysis buffer (1 mM Tris-HCl [pH 7.4], 1 mM NaCl, 300 µM $MgCl_2$, 0.01% Tween-20, 0.01% IGEPAL CA-630, 0.001% Digitonin, 0.1% BSA, 100 µM DTT, and 100 mU/µL RNase inhibitor) for 1 minute on ice, washed twice in 500 µL of wash buffer (1 mM Tris-HCl [pH 7.4], 1 mM NaCl, 300 µM $MgCl_2$, 0.01% Tween-20, 0.1% BSA, 100 µM DTT, and 100 mU/µL RNase inhibitor), and the number of nuclei was assessed using the Countess II FL Automated Cell Counter (ThermoFisher). Thereafter, approximately 16,000 nuclei were incubated with the transposase enzyme, loaded into Chromium Next GEM Chip H Single Cell Kit (10x Genomics). snATAC libraries were generated using Chromium Single Cell ATAC Reagent Kits User Guide v1.1 (10x Genomics) according to manufacturer’s instructions; for the multi-omics samples, nuclei were loaded into Chromium Next GEM Chip J Single Cell Kit (10x Genomics); libraries were prepared using Chromium Next GEM Single Cell Multiome ATAC + Gene Expression Reagent Kits (10x Genomics) according to manufacturer’s instructions. The quality of the libraries was checked on the Agilent Bioanalyzer with High Sensitivity DNA kit (Agilent); per sample libraries were sequenced on Illumina Novaseq 6000 with target sequencing depths of 25,000 - 70,000 reads per nucleus.

For single-cell (sc)RNAseq, cells were counted using a hemocytometer, 10,000 cells were loaded into Chromium Next GEM Chip G Single Cell Kit (10x Genomics), and scRNA libraries were generated with Chromium Single Cell 3' Reagent Kits v3.1 (10x Genomics) according to manufacturer’s instructions. The quality of the libraries was checked on the 4200 Agilent Tapestation with High Sensitivity DNA kit (Agilent); per sample libraries were sequenced on Illumina Novaseq 6000 with target sequencing depths of 30,000 - 65,000 reads per cell.

Single-cell transcriptomics/ epigenetics data pre-processing

Standard CellRanger pipeline (6.1.2) and CellRanger ARC (2.0.0) were applied for aligning reads to the aforementioned version of the *H sapiens* genome and for quantifying gene/ peak expression. For the RNA component, intron-matching reads contributed to the gene

1100 expression levels. The processed gene expression matrix was imported in Seurat.[126]
1101 Additional filtering was performed on the distributions summarizing the number of counts,
1102 features, and percentages of reads incident to mitochondrial and ribosomal genes, across
1103 cells, per sample (accepted cells satisfied the criteria: number of UMIs > 8,000, number of
1104 genes per cell > 1,000, $\log_{10}$ (genes per UMI) > 0.75). We observed different ranges for MT
1105 and RP proportions for the scRNAseq and snRNAseq samples, respectively (we retained cells
1106 with 15-40% RP [scRNAseq] and 2-25% RP [snRNAseq]). Post-filtering, on all retained cells,
1107 the MT and RP entries were excluded from the expression matrix, pre-normalization. The
1108 normalization of expression levels was based on $\log_2$ normalization (scale.factor = 10000).
1109 The cell cycle assignation was performed in Seurat using the 'CellCycleScoring' function and
1110 *a priori* defined gene set.
1111
1112 **Clustering**
1113 Next, we applied the ClustAssess framework to determine optimal, data-driven parameters,
1114 starting with the number and type features according the stability of resulting partitions.[70] We
1115 used Element-centric similarity,[70] summarized on 30 iterations into Element centric
1116 consistency (ECC),[71] to objectively assess stability.[126] Highly variable features (N=1,000
1117 determined using the vst) approach, yielded optimal outputs. A 20-shared nearest neighbour
1118 (SNN) graph was constructed on the HGV PCA.[126] To address batch effect across sc and sn
1119 quantifications, we applied Harmony.[127] Clustering was performed using Louvain approach
1120 (resolution=0.2), implemented within Seurat[126] v4.0.5. 8 clusters produced a stable partition
1121 on scRNAseq and snRNAseq components. We excluded the smallest cluster (133 driven by
1122 a specific sample (i.e. C1-specific cluster). A X^2 test was used to assess the significance of
1123 proportions of cells for PMS *vs* control samples. Marker genes (on cluster *vs* complement and
1124 pairwise differential expression) were identified using the 'findMarker' function. The top 5 most
1125 positively differentially expressed genes were visualized in a heatmap.
1126 Enrichment analyses were performed using gprofiler[128] on markers called on a Wilcox test
1127 with a $|\log_2(FC)|$ threshold of 0.25, an adjusted p-value (Benjamini Hochberg multiple testing
1128 correction) less than 0.05 and a minimum percentage of cells expressing the gene of 0.1, in
1129 either subset. The background set for the enrichment analysis comprised all genes expressed
1130 in at least 10 cells.
1131
1132 **Voting Schemes**
1133 A variable voting-scheme was used to identify cell subsets requiring a minimum number of
1134 expressed genes corroborated with a minimum average expression level. The voting scheme
1135 for radial glial gene signature includes cells expressing 6 out of 9 manually curated genes
1136 (**Table S4**) with a normalized expression threshold of 1; glial progenitor cells express 7 out of

10 genes (**Table S4**) with an expression threshold of 0.5; neural progenitor cells express 5 out of 7 genes (**Table S4**) with an expression threshold of 0.5. The voting scheme for IFNα/β signalling is based on cells expressing 3 out of 6 genes (**Table S4**) with an expression threshold of 0.5; NOTCH1 signalling comprises cells expressing 13 out of 16 genes (**Table S4**) with no abundance threshold (I.e. presence/ absence).

Re-analysis of *Absinta et al.* and *Schirmer et al.* Data ex vivo datasets

Raw fastQ files from the studies by *Schirmer et al.* (2019)[77] and *Absinta et al.* (2021)[16] were downloaded from ENA using fasterq-dump. The quality checking and mapping leading to the filtered feature-barcode matrices were performed as described above. For the *Schirmer et al.* (2019) dataset, cells with less than 4,000 features/genes were retained; an upper bound of 15,000 was employed for the maximum number of UMIs per cell; 5% is maximum proportion of fragments incident to mitochondrial DNA; 10% is the maximum proportion of reads incident to nuclear ribosomal genes. For *Absinta et al.* (2021), cells with the number of features between 200 and 5000 were kept for subsequent steps of the analysis; an upper threshold of 20,000 UMI counts was used, and the maximum mt% was set to 5%. Both datasets were normalized using SCTransform;[129] the *Absinta et al.* (2021) dataset was batch corrected using Harmony[127] on the patient variable, with θ = 2. To detect stable partitions, on each separate dataset, ClustAssess[70] was used with 20-50 iterations, assessing resolution parameters between 0.1 and 1.5 (0.1 increment steps). For the *Schirmer et al.* (2019) dataset, the top 4500 highly variable features yielded the most stable partitions; for the *Absinta et al.* (2021) dataset the top 3,500 highly variable features were selected. For both, the optimal resolution value was 0.6.

Pseudotime Analysis

Monocle3[130] was used to infer trajectories for the *in vitro* data, as well as for the single-cell data from the *Schirmer et al.* and *Absinta et al*. studies. To identify the start and the endpoint, a selection of genes was used in a voting approach. The manually curated set of genes, used for determining the starting region in the *in vitro* data, comprises TOP2A, CENPF, UBE2C, ASPM, APOLD1 with an expression threshold of 2 and a tolerance of 1 gene, i.e. any one gene from the set maybe not expressed; for the ending region, genes IFIT2 and CDKN2A were used, with an expression threshold of 1.5 and a tolerance of 0.

For the *Absinta et al.* and *Schirmer et al.*, larger subsets of genes were used; for the former, the following genes were used for the starting region: *LY6E*, *PPAN*, *FASN*, *CLU, SORD*, *TRAP1*, *TUBB2A*, *AP1S2*, *YBX3*, with an expression threshold of 0.5 and a tolerance of 4 genes; for the ending region, the following genes were used *ISG15*, *B4GALT5*, *IFITM3*, *SAR1A*, *KIAA1217*, *TRPC4*, *FGF4*, *B2M*, *ZC3HAV1*, *WARS*, *FN1*, *IFIT1*, with an expression

1174 threshold of 0.5 and a tolerance of 4 genes missing. For the *Schirmer et al* dataset, the ending
1175 region was defined by genes *ISG15*, *B4GALT5*, *IFITM3*, *SAR1A*, *KIAA1217*, *TRPC4*, *FGF4*,
1176 *B2M*, *ZC3HAV1*, *WARS*, *DDX58*, with an expression threshold of 0.5 and a tolerance of 6
1177 genes.
1178 Using the ordering of cells based on their transcriptomic signatures, the ClustAssess stability
1179 framework was applied on gene expression levels. This yielded a stable number of gene-
1180 clusters, named gene modules, representing a precursor of GRN inference; the genes per
1181 module were further characterized from a pathway perspective (using gprofiler[128]), against GO
1182 terms, KEGG and REAC terms, and functional elements (TFs and miRNAs). Next, we chose
1183 three gene modules that characterized sections of interest on the trajectory-based UMAPs of
1184 the *in vitro* dataset. The genes within each module were used to create a proxy (a
1185 transcriptomic pattern) subsequently employed to identify homologue gene modules
1186 computed based on the *ex vivo* datasets, *Schirmer et al.* and *Absinta et al.,* respectively.
1187 Briefly, we considered the percentage of genes present in the *ex vivo* gene modules using the
1188 three *in vitro* gene modules; to account for the variable number of genes for bo*th in vitro* and
1189 *ex vivo* modules the outputs are scaled by the size of the gene set, i.e. larger gene sets are
1190 penalized more than smaller gene sets. The pairwise comparison of gene modules (**Fig. S4A-**
1191 **D**) relies on Fisher's exact tests, using the *in vitro* data as baseline comparator. Benjamini-
1192 Hochber (FDR) correction was applied to account for the multiple testing pyscenic[131] was used
1193 to infer regulatory interactions, aligned with the metadata available for the *Homo sapiens*
1194 (hg38) reference genome. A docker container was used to generate a loom object from the
1195 existing Seurat object. Loompy was used[132] to create a SCope object, explored using the
1196 SCope web application; figure 6G illustrates specific regulons.
1197
1198 **Cell-cell regulatory interactions and effects**
1199 NicheNet[80] (v 2.0.4) was used to predict intercellular regulatory interactions, based on ligand-
1200 receptor databases (weighted_networks_nsga2r_final.rds). The correlative analysis,
1201 summarized as interaction scores, was applied on cluster-specific marker genes (differentially
1202 expressed genes). Further analyses were focused on cluster 5 ("inflammatory cluster")
1203 assigned as sender cells *vs* receiver cells, as the remaining clusters, respectively. The
1204 analysis was performed separately on control and PMS iNSCs, respectively. The summary of
1205 interactions was visualized using circos plot (circlize library v.0.4.15).
1206
1207 **Cytokine Array**
1208 iNSCs were plated at a density of 100,000 cells/cm^2 on GFR-coated plates. Media was
1209 collected on day 5 from each line. The Human Cytokine Antibody Array C5 (RayBiotech) was
1210 used for semi quantitative detection of 80 proteins according to manufacturer's instructions.

1211 Overnight incubation was performed for steps when the option was given. Membranes were
1212 exposed using a Gel Doc XR imager (BioRad). Blots were analyzed using the Protein Array
1213 Analyzer macro for ImageJ (written by Gilles Carpentier, 2008). The relative quantity of each
1214 protein was normalized to the positive and negative controls included on the array. The array
1215 was performed once for each iNSC line. Control lines were averaged together to generate a
1216 fold change comparison over PMS iNSC lines. To visualize the results, we calculate the Z-
1217 score per cytokine using the heatmap function in an R environment.
1218

1219 **snATACseq analysis**

1220 CellRanger ARC2.0.0 (multi-omics) and CellRanger ATAC2.0.0 (snATAC only) were used to
1221 map reads and quantify expression for the single nuclei ATAC-seq datasets. The peak calling
1222 was performed on pseudobulked input, comprising cells with at least 100 reads sequencing
1223 depth. Union peaks (peaks present in at least one sample) were reported. We excluded peaks
1224 overlapping the ENCODE-defined blacklist regions (hg38). To address the variation in
1225 sequencing depths, across samples, we normalized expression levels using random
1226 subsampling without replacement.[110] The set of fragments (with lengths varying from 200 to
1227 400 nts) *vs* the union-peaks were used to generate the ATAC expression matrix. For
1228 downstream analysis we relied onSeurat[126], Signac[133], and ArchR[134] packages. Additional
1229 quality controls include assessment of nucleosome signatures and TSS enrichment analysis.
1230 we filtered the fragments with nucleosome signals < 4 and TSS enrichment levels > 2. Peak
1231 intensities were normalized using the term frequency inverse document frequency (TF-IDF)
1232 normalization (scale factor = 10,000). The dimensionality reduction was performed using latent
1233 semantic indexing (LSI). Additionally, we performed Harmony integration across batches,
1234 which was used as input for the final clustering (resolution=0.2, SLM method[126]). Differentially
1235 expressed peaks were identified using the 'findMarker' function (Seurat package). We
1236 performed *de novo* motif analysis using Homer (*findMotifsGenome.pl*) and GO term
1237 enrichment analysis using GREAT with the background of the whole genome.[135]
1238

1239 **Integrative analysis of multimaps profiles**

1240 The integration of snRNAseq and snATACseq signals was performed on 5,242 cells with
1241 matched barcodes. The crosstalk between modalities was assessed using the partitioning
1242 information obtained on single modalities. The co-variation in expressed was summarized in
1243 joint ATAC/RNA heatmaps, with Z scores, calculated per modality, on pseudobulked
1244 expression per gene being presented for the gene itself (RNA modality), TSS proximal peaks
1245 (<3kb) and TSS distal peaks (greater than 3kb and less than 50kb). Both ATAC and RNA
1246 modalities were used to infer regulons using SCENIC+.[136]
1247

1248 **Statistical analysis**

1249 For all phenotypic analyses, a p-value < 0.05 was considered significant (*). We performed
1250 statistical tests described in individual figure legends using Prism software version 10
1251 (GraphPad Software, San Diego CA). A Benjamini-Hochberg, False discovery rate (FDR)
1252 multiple testing correction was applied to account for Type I errors. For low throughput
1253 differential expression analysis on genes, we used a negative binomial test with the FDR cutoff
1254 value set to <0.05.

1255 All analyses were performed on R 4.2.3, on high memory computer (MacPro M1 Max, 64GB
1256 memory) and servers (Intel E7-8860v4, 3TB memory).

1257

REFERENCES

1. Reich, D.S., Lucchinetti, C.F., and Calabresi, P.A. (2018). Multiple Sclerosis. N Engl J Med *378*, 169-180. 10.1056/NEJMra1401483.

2. Giovannoni, G., Popescu, V., Wuerfel, J., Hellwig, K., Iacobaeus, E., Jensen, M.B., Garcia-Dominguez, J.M., Sousa, L., De Rossi, N., Hupperts, R., et al. (2022). Smouldering multiple sclerosis: the 'real MS'. Ther Adv Neurol Disord *15*, 17562864211066751. 10.1177/17562864211066751.

3. Graves, J.S., Krysko, K.M., Hua, L.H., Absinta, M., Franklin, R.J.M., and Segal, B.M. (2023). Ageing and multiple sclerosis. Lancet Neurol *22*, 66-77. 10.1016/S1474-4422(22)00184-3.

4. Hou, Y., Dan, X., Babbar, M., Wei, Y., Hasselbalch, S.G., Croteau, D.L., and Bohr, V.A. (2019). Ageing as a risk factor for neurodegenerative disease. Nat Rev Neurol *15*, 565-581. 10.1038/s41582-019-0244-7.

5. Papadopoulos, D., Magliozzi, R., Mitsikostas, D.D., Gorgoulis, V.G., and Nicholas, R.S. (2020). Aging, Cellular Senescence, and Progressive Multiple Sclerosis. Front Cell Neurosci *14*, 178. 10.3389/fncel.2020.00178.

6. Tian, Y.E., Cropley, V., Maier, A.B., Lautenschlager, N.T., Breakspear, M., and Zalesky, A. (2023). Heterogeneous aging across multiple organ systems and prediction of chronic disease and mortality. Nat Med *29*, 1221-1231. 10.1038/s41591-023-02296-6.

7. Cole, J.H., Raffel, J., Friede, T., Eshaghi, A., Brownlee, W.J., Chard, D., De Stefano, N., Enzinger, C., Pirpamer, L., Filippi, M., et al. (2020). Longitudinal Assessment of Multiple Sclerosis with the Brain-Age Paradigm. Ann Neurol *88*, 93-105. 10.1002/ana.25746.

8. Liao, Q., He, J., Tian, F.F., Bi, F.F., and Huang, K. (2022). A causal relationship between leukocyte telomere length and multiple sclerosis: A Mendelian randomization study. Front Immunol *13*, 922922. 10.3389/fimmu.2022.922922.

9. Krysko, K.M., Henry, R.G., Cree, B.A.C., Lin, J., University of California, S.F.M.S.E.T., Caillier, S., Santaniello, A., Zhao, C., Gomez, R., Bevan, C., et al. (2019). Telomere Length Is Associated with Disability Progression in Multiple Sclerosis. Ann Neurol *86*, 671-682. 10.1002/ana.25592.

10. Buhring, J., Hecker, M., Fitzner, B., and Zettl, U.K. (2021). Systematic Review of Studies on Telomere Length in Patients with Multiple Sclerosis. Aging Dis *12*, 1272-1286. 10.14336/AD.2021.0106.

11. Haider, L., Fischer, M.T., Frischer, J.M., Bauer, J., Hoftberger, R., Botond, G., Esterbauer, H., Binder, C.J., Witztum, J.L., and Lassmann, H. (2011). Oxidative damage in multiple sclerosis lesions. Brain *134*, 1914-1924. 10.1093/brain/awr128.

12. Dutta, R., McDonough, J., Yin, X., Peterson, J., Chang, A., Torres, T., Gudz, T., Macklin, W.B., Lewis, D.A., Fox, R.J., et al. (2006). Mitochondrial dysfunction as a cause of axonal degeneration in multiple sclerosis patients. Ann Neurol *59*, 478-489. 10.1002/ana.20736.

13. Campbell, G.R., Ziabreva, I., Reeve, A.K., Krishnan, K.J., Reynolds, R., Howell, O., Lassmann, H., Turnbull, D.M., and Mahad, D.J. (2011). Mitochondrial DNA deletions and neurodegeneration in multiple sclerosis. Ann Neurol *69*, 481-492. 10.1002/ana.22109.

14. Kular, L., Klose, D., Urdanoz-Casado, A., Ewing, E., Planell, N., Gomez-Cabrero, D., Needhamsen, M., and Jagodic, M. (2022). Epigenetic clock indicates accelerated aging in glial cells of progressive multiple sclerosis patients. Front Aging Neurosci *14*, 926468. 10.3389/fnagi.2022.926468.

15. Choi, I.Y., Lee, P., Adany, P., Hughes, A.J., Belliston, S., Denney, D.R., and Lynch, S.G. (2018). In vivo evidence of oxidative stress in brains of patients with progressive multiple sclerosis. Mult Scler *24*, 1029-1038. 10.1177/1352458517711568.

16. Absinta, M., Maric, D., Gharagozloo, M., Garton, T., Smith, M.D., Jin, J., Fitzgerald, K.C., Song, A., Liu, P., Lin, J.P., et al. (2021). A lymphocyte-microglia-astrocyte axis in chronic active multiple sclerosis. Nature. 10.1038/s41586-021-03892-7.

17. Nicaise, A.M., Wagstaff, L.J., Willis, C.M., Paisie, C., Chandok, H., Robson, P., Fossati, V., Williams, A., and Crocker, S.J. (2019). Cellular senescence in progenitor cells contributes to diminished remyelination potential in progressive multiple sclerosis. Proc Natl Acad Sci U S A *116*, 9030-9039. 10.1073/pnas.1818348116.

18. Jokubaitis, V.G., Campagna, M.P., Ibrahim, O., Stankovich, J., Kleinova, P., Matesanz, F., Hui, D., Eichau, S., Slee, M., Lechner-Scott, J., et al. (2022). Not all roads lead to the immune system: the genetic basis of multiple sclerosis severity. Brain. 10.1093/brain/awac449.

19. Lopez-Otin, C., Blasco, M.A., Partridge, L., Serrano, M., and Kroemer, G. (2023). Hallmarks of aging: An expanding universe. Cell *186*, 243-278. 10.1016/j.cell.2022.11.001.

20. Studer, L., Vera, E., and Cornacchia, D. (2015). Programming and Reprogramming Cellular Age in the Era of Induced Pluripotency. Cell Stem Cell *16*, 591-600. 10.1016/j.stem.2015.05.004.

21. Kabacik, S., Lowe, D., Fransen, L., Leonard, M., Ang, S.-L., Whiteman, C., Corsi, S., Cohen, H., Felton, S., Bali, R., et al. (2022). The relationship between epigenetic age and the hallmarks of aging in human cells. Nature Aging *2*, 484-493. 10.1038/s43587-022-00220-0.

22. Chomyk, A.M., Volsko, C., Tripathi, A., Deckard, S.A., Trapp, B.D., Fox, R.J., and Dutta, R. (2017). DNA methylation in demyelinated multiple sclerosis hippocampus. Sci Rep *7*, 8696. 10.1038/s41598-017-08623-5.

23. Huynh, J.L., Garg, P., Thin, T.H., Yoo, S., Dutta, R., Trapp, B.D., Haroutunian, V., Zhu, J., Donovan, M.J., Sharp, A.J., and Casaccia, P. (2014). Epigenome-wide differences in pathology-free regions of multiple sclerosis-affected brains. Nat Neurosci *17*, 121-130. 10.1038/nn.3588.

24. Mutukula, N., Man, Z., Takahashi, Y., Iniesta Martinez, F., Morales, M., Carreon-Guarnizo, E., Hernandez Clares, R., Garcia-Bernal, D., Martinez Martinez, L., Lajara, J., et al. (2021). Generation of RRMS and PPMS specific iPSCs as a platform for modeling Multiple Sclerosis. Stem Cell Res *53*, 102319. 10.1016/j.scr.2021.102319.

25. Ghirotto, B., Oliveira, D.F., Cipelli, M., Basso, P.J., de Lima, J., Breda, C.N.S., Ribeiro, H.C., Silva, C.C.C., Sertie, A.L., Oliveira, A.E.R., et al. (2022). MS-Driven Metabolic Alterations Are Recapitulated in iPSC-Derived Astrocytes. Ann Neurol *91*, 652-669. 10.1002/ana.26336.

26. Clayton, B.L.L., Barbar, L., Sapar, M., Rusielewicz, T., Kalpana, K., Migliori, B., Team, N.G.S.C.A., Paull, D., Brenner, K., Moroziewicz, D., et al. (2023). Patient iPSC models reveal glia-intrinsic phenotypes in multiple sclerosis. bioRxiv. 10.1101/2023.08.01.551553.

27. Obernier, K., and Alvarez-Buylla, A. (2019). Neural stem cells: origin, heterogeneity and regulation in the adult mammalian brain. Development *146*. 10.1242/dev.156059.

28. Gould, E., Reeves, A.J., Graziano, M.S., and Gross, C.G. (1999). Neurogenesis in the neocortex of adult primates. Science *286*, 548-552. 10.1126/science.286.5439.548.
29. Ponti, G., Peretto, P., and Bonfanti, L. (2008). Genesis of neuronal and glial progenitors in the cerebellar cortex of peripuberal and adult rabbits. PLoS One *3*, e2366. 10.1371/journal.pone.0002366.
30. Jhaveri, D.J., Tedoldi, A., Hunt, S., Sullivan, R., Watts, N.R., Power, J.M., Bartlett, P.F., and Sah, P. (2018). Evidence for newly generated interneurons in the basolateral amygdala of adult mice. Mol Psychiatry *23*, 521-532. 10.1038/mp.2017.134.
31. Ernst, A., Alkass, K., Bernard, S., Salehpour, M., Perl, S., Tisdale, J., Possnert, G., Druid, H., and Frisen, J. (2014). Neurogenesis in the striatum of the adult human brain. Cell *156*, 1072-1083. 10.1016/j.cell.2014.01.044.
32. Navarro Negredo, P., Yeo, R.W., and Brunet, A. (2020). Aging and Rejuvenation of Neural Stem Cells and Their Niches. Cell Stem Cell *27*, 202-223. 10.1016/j.stem.2020.07.002.
33. Encinas, J.M., Michurina, T.V., Peunova, N., Park, J.H., Tordo, J., Peterson, D.A., Fishell, G., Koulakov, A., and Enikolopov, G. (2011). Division-coupled astrocytic differentiation and age-related depletion of neural stem cells in the adult hippocampus. Cell Stem Cell *8*, 566-579. 10.1016/j.stem.2011.03.010.
34. Culig, L., Chu, X., and Bohr, V.A. (2022). Neurogenesis in aging and age-related neurodegenerative diseases. Ageing Res Rev *78*, 101636. 10.1016/j.arr.2022.101636.
35. Knoth, R., Singec, I., Ditter, M., Pantazis, G., Capetian, P., Meyer, R.P., Horvat, V., Volk, B., and Kempermann, G. (2010). Murine features of neurogenesis in the human hippocampus across the lifespan from 0 to 100 years. PLoS One *5*, e8809. 10.1371/journal.pone.0008809.
36. Wang, C., Liu, F., Liu, Y.Y., Zhao, C.H., You, Y., Wang, L., Zhang, J., Wei, B., Ma, T., Zhang, Q., et al. (2011). Identification and characterization of neuroblasts in the subventricular zone and rostral migratory stream of the adult human brain. Cell Res *21*, 1534-1550. 10.1038/cr.2011.83.
37. Gonzalez-Perez, O. (2012). Neural stem cells in the adult human brain. Biol Biomed Rep *2*, 59-69.
38. Sorrells, S.F., Paredes, M.F., Cebrian-Silla, A., Sandoval, K., Qi, D., Kelley, K.W., James, D., Mayer, S., Chang, J., Auguste, K.I., et al. (2018). Human hippocampal neurogenesis drops sharply in children to undetectable levels in adults. Nature *555*, 377-381. 10.1038/nature25975.
39. Tobin, M.K., Musaraca, K., Disouky, A., Shetti, A., Bheri, A., Honer, W.G., Kim, N., Dawe, R.J., Bennett, D.A., Arfanakis, K., and Lazarov, O. (2019). Human Hippocampal Neurogenesis Persists in Aged Adults and Alzheimer's Disease Patients. Cell Stem Cell *24*, 974-982 e973. 10.1016/j.stem.2019.05.003.
40. Hagihara, H., Murano, T., Ohira, K., Miwa, M., Nakamura, K., and Miyakawa, T. (2019). Expression of progenitor cell/immature neuron markers does not present definitive evidence for adult neurogenesis. Mol Brain *12*, 108. 10.1186/s13041-019-0522-8.
41. Sirko, S., Schichor, C., Della Vecchia, P., Metzger, F., Sonsalla, G., Simon, T., Burkle, M., Kalpazidou, S., Ninkovic, J., Masserdotti, G., et al. (2023). Injury-specific factors in the cerebrospinal fluid regulate astrocyte plasticity in the human brain. Nat Med *29*, 3149-3161. 10.1038/s41591-023-02644-6.

42. Snethen, H., Love, S., and Scolding, N. (2008). Disease-responsive neural precursor cells are present in multiple sclerosis lesions. Regen Med *3*, 835-847. 10.2217/17460751.3.6.835.
43. Nait-Oumesmar, B., Picard-Riera, N., Kerninon, C., Decker, L., Seilhean, D., Hoglinger, G.U., Hirsch, E.C., Reynolds, R., and Baron-Van Evercooren, A. (2007). Activation of the subventricular zone in multiple sclerosis: evidence for early glial progenitors. Proc Natl Acad Sci U S A *104*, 4694-4699. 10.1073/pnas.0606835104.
44. Wang, H., Yang, Y., Liu, J., and Qian, L. (2021). Direct cell reprogramming: approaches, mechanisms and progress. Nat Rev Mol Cell Biol *22*, 410-424. 10.1038/s41580-021-00335-z.
45. Meyer, S., Worsdorfer, P., Gunther, K., Thier, M., and Edenhofer, F. (2015). Derivation of Adult Human Fibroblasts and their Direct Conversion into Expandable Neural Progenitor Cells. J Vis Exp, e52831. 10.3791/52831.
46. Ionescu, R.-B., Nicaise, A.M., Reisz, J.A., Williams, E.C., Prasad, P., Dzieciatkowska, M., Stephenson, D., Cubero, M.S., Pirvan, L., Willis, C.M., et al. (2024). Increased Cholesterol Synthesis Drives Neurotoxicity in Patient Stem Cell-Derived Model of Multiple Sclerosis. bioRxiv, 2024.2001.2016.575826. 10.1101/2024.01.16.575826.
47. Moutsopoulos, I., Williams, E.C., and Mohorianu, II (2023). bulkAnalyseR: an accessible, interactive pipeline for analysing and sharing bulk multi-modal sequencing data. Brief Bioinform *24*. 10.1093/bib/bbac591.
48. Moutsopoulos, I., Maischak, L., Lauzikaite, E., Vasquez Urbina, S.A., Williams, E.C., Drost, H.G., and Mohorianu, II (2021). noisyR: enhancing biological signal in sequencing datasets by characterizing random technical noise. Nucleic Acids Res *49*, e83. 10.1093/nar/gkab433.
49. Love, M.I., Huber, W., and Anders, S. (2014). Moderated estimation of fold change and dispersion for RNA-seq data with DESeq2. Genome Biol *15*, 550. 10.1186/s13059-014-0550-8.
50. Robinson, M.D., McCarthy, D.J., and Smyth, G.K. (2010). edgeR: a Bioconductor package for differential expression analysis of digital gene expression data. Bioinformatics *26*, 139-140. 10.1093/bioinformatics/btp616.
51. Raudvere, U., Kolberg, L., Kuzmin, I., Arak, T., Adler, P., Peterson, H., and Vilo, J. (2019). g:Profiler: a web server for functional enrichment analysis and conversions of gene lists (2019 update). Nucleic Acids Res *47*, W191-W198. 10.1093/nar/gkz369.
52. Frisch, S.M., and MacFawn, I.P. (2020). Type I interferons and related pathways in cell senescence. Aging Cell *19*, e13234. 10.1111/acel.13234.
53. Park, H., Kim, C.H., Jeong, J.H., Park, M., and Kim, K.S. (2016). GDF15 contributes to radiation-induced senescence through the ROS-mediated p16 pathway in human endothelial cells. Oncotarget *7*, 9634-9644. 10.18632/oncotarget.7457.
54. Moiseeva, V., Cisneros, A., Sica, V., Deryagin, O., Lai, Y., Jung, S., Andres, E., An, J., Segales, J., Ortet, L., et al. (2023). Senescence atlas reveals an aged-like inflamed niche that blunts muscle regeneration. Nature *613*, 169-178. 10.1038/s41586-022-05535-x.
55. Huang, W., Hickson, L.J., Eirin, A., Kirkland, J.L., and Lerman, L.O. (2022). Cellular senescence: the good, the bad and the unknown. Nat Rev Nephrol *18*, 611-627. 10.1038/s41581-022-00601-z.
56. Shireby, G.L., Davies, J.P., Francis, P.T., Burrage, J., Walker, E.M., Neilson, G.W.A., Dahir, A., Thomas, A.J., Love, S., Smith, R.G., et al. (2020). Recalibrating the epigenetic clock: implications for assessing biological age in the human cortex. Brain *143*, 3763-3775. 10.1093/brain/awaa334.

57. Horvath, S. (2013). DNA methylation age of human tissues and cell types. Genome Biol *14*, R115. 10.1186/gb-2013-14-10-r115.
58. Zhang, Q., Vallerga, C.L., Walker, R.M., Lin, T., Henders, A.K., Montgomery, G.W., He, J., Fan, D., Fowdar, J., Kennedy, M., et al. (2019). Improved precision of epigenetic clock estimates across tissues and its implication for biological ageing. Genome Med *11*, 54. 10.1186/s13073-019-0667-1.
59. Dolatabadi, S., Jonasson, E., Andersson, L., Luna Santamaria, M., Linden, M., Osterlund, T., Aman, P., and Stahlberg, A. (2022). FUS-DDIT3 Fusion Oncoprotein Expression Affects JAK-STAT Signaling in Myxoid Liposarcoma. Front Oncol *12*, 816894. 10.3389/fonc.2022.816894.
60. Kidani, Y., Elsaesser, H., Hock, M.B., Vergnes, L., Williams, K.J., Argus, J.P., Marbois, B.N., Komisopoulou, E., Wilson, E.B., Osborne, T.F., et al. (2013). Sterol regulatory element-binding proteins are essential for the metabolic programming of effector T cells and adaptive immunity. Nat Immunol *14*, 489-499. 10.1038/ni.2570.
61. Hennighausen, L., and Robinson, G.W. (2008). Interpretation of cytokine signaling through the transcription factors STAT5A and STAT5B. Genes Dev *22*, 711-721. 10.1101/gad.1643908.
62. Bailey, C.M., Abbott, D.E., Margaryan, N.V., Khalkhali-Ellis, Z., and Hendrix, M.J. (2008). Interferon regulatory factor 6 promotes cell cycle arrest and is regulated by the proteasome in a cell cycle-dependent manner. Mol Cell Biol *28*, 2235-2243. 10.1128/MCB.01866-07.
63. Nyati, K.K., and Kishimoto, T. (2021). Recent Advances in the Role of Arid5a in Immune Diseases and Cancer. Front Immunol *12*, 827611. 10.3389/fimmu.2021.827611.
64. International Multiple Sclerosis Genetics, C. (2019). Multiple sclerosis genomic map implicates peripheral immune cells and microglia in susceptibility. Science *365*. 10.1126/science.aav7188.
65. International Multiple Sclerosis Genetics, C. (2013). Network-based multiple sclerosis pathway analysis with GWAS data from 15,000 cases and 30,000 controls. Am J Hum Genet *92*, 854-865. 10.1016/j.ajhg.2013.04.019.
66. Hussman, J.P., Beecham, A.H., Schmidt, M., Martin, E.R., McCauley, J.L., Vance, J.M., Haines, J.L., and Pericak-Vance, M.A. (2016). GWAS analysis implicates NF-kappaB-mediated induction of inflammatory T cells in multiple sclerosis. Genes Immun *17*, 305-312. 10.1038/gene.2016.23.
67. Kristjansdottir, G., Sandling, J.K., Bonetti, A., Roos, I.M., Milani, L., Wang, C., Gustafsdottir, S.M., Sigurdsson, S., Lundmark, A., Tienari, P.J., et al. (2008). Interferon regulatory factor 5 (IRF5) gene variants are associated with multiple sclerosis in three distinct populations. J Med Genet *45*, 362-369. 10.1136/jmg.2007.055012.
68. Hatami, M., Salmani, T., Arsang-Jang, S., Davood Omrani, M., Mazdeh, M., Ghafouri-Fard, S., Sayad, A., and Taheri, M. (2018). STAT5a and STAT6 gene expression levels in multiple sclerosis patients. Cytokine *106*, 108-113. 10.1016/j.cyto.2017.10.022.
69. Shang, Z., Sun, W., Zhang, M., Xu, L., Jia, X., Zhang, R., and Fu, S. (2020). Identification of key genes associated with multiple sclerosis based on gene expression data from peripheral blood mononuclear cells. PeerJ *8*, e8357. 10.7717/peerj.8357.
70. Shahsavari, A., Munteanu, A., and Mohorianu, I. (2022). ClustAssess: tools for assessing the robustness of single-cell clustering. bioRxiv, 2022.2001.2031.478592. 10.1101/2022.01.31.478592.

71. Gates, A.J., Wood, I.B., Hetrick, W.P., and Ahn, Y.Y. (2019). Element-centric clustering comparison unifies overlaps and hierarchy. Sci Rep *9*, 8574. 10.1038/s41598-019-44892-y.

72. Eze, U.C., Bhaduri, A., Haeussler, M., Nowakowski, T.J., and Kriegstein, A.R. (2021). Single-cell atlas of early human brain development highlights heterogeneity of human neuroepithelial cells and early radial glia. Nat Neurosci *24*, 584-594. 10.1038/s41593-020-00794-1.

73. Chamling, X., Kallman, A., Fang, W., Berlinicke, C.A., Mertz, J.L., Devkota, P., Pantoja, I.E.M., Smith, M.D., Ji, Z., Chang, C., et al. (2021). Single-cell transcriptomic reveals molecular diversity and developmental heterogeneity of human stem cell-derived oligodendrocyte lineage cells. Nat Commun *12*, 652. 10.1038/s41467-021-20892-3.

74. Marques, S., van Bruggen, D., Vanichkina, D.P., Floriddia, E.M., Munguba, H., Varemo, L., Giacomello, S., Falcao, A.M., Meijer, M., Bjorklund, A.K., et al. (2018). Transcriptional Convergence of Oligodendrocyte Lineage Progenitors during Development. Dev Cell *46*, 504-517 e507. 10.1016/j.devcel.2018.07.005.

75. Darmanis, S., Sloan, S.A., Zhang, Y., Enge, M., Caneda, C., Shuer, L.M., Hayden Gephart, M.G., Barres, B.A., and Quake, S.R. (2015). A survey of human brain transcriptome diversity at the single cell level. Proc Natl Acad Sci U S A *112*, 7285-7290. 10.1073/pnas.1507125112.

76. Luciani, M., Garsia, C., Beretta, S., Petiti, L., Peano, C., Merelli, I., Cifola, I., Miccio, A., Meneghini, V., and Gritti, A. (2023). Human iPSC-derived neural stem cells display a radial glia-like signature in vitro and favorable long-term safety in transplanted mice. bioRxiv, 2023.2008.2004.551937. 10.1101/2023.08.04.551937.

77. Schirmer, L., Velmeshev, D., Holmqvist, S., Kaufmann, M., Werneburg, S., Jung, D., Vistnes, S., Stockley, J.H., Young, A., Steindel, M., et al. (2019). Neuronal vulnerability and multilineage diversity in multiple sclerosis. Nature *573*, 75-82. 10.1038/s41586-019-1404-z.

78. Saul, D., Kosinsky, R.L., Atkinson, E.J., Doolittle, M.L., Zhang, X., LeBrasseur, N.K., Pignolo, R.J., Robbins, P.D., Niedernhofer, L.J., Ikeno, Y., et al. (2022). A new gene set identifies senescent cells and predicts senescence-associated pathways across tissues. Nat Commun *13*, 4827. 10.1038/s41467-022-32552-1.

79. Johnson, C.A., and Ghashghaei, H.T. (2020). Sp2 regulates late neurogenic but not early expansive divisions of neural stem cells underlying population growth in the mouse cortex. Development *147*. 10.1242/dev.186056.

80. Browaeys, R., Saelens, W., and Saeys, Y. (2020). NicheNet: modeling intercellular communication by linking ligands to target genes. Nat Methods *17*, 159-162. 10.1038/s41592-019-0667-5.

81. Imayoshi, I., Sakamoto, M., Yamaguchi, M., Mori, K., and Kageyama, R. (2010). Essential roles of Notch signaling in maintenance of neural stem cells in developing and adult brains. J Neurosci *30*, 3489-3498. 10.1523/JNEUROSCI.4987-09.2010.

82. Borghi, A., Verstrepen, L., and Beyaert, R. (2016). TRAF2 multitasking in TNF receptor-induced signaling to NF-kappaB, MAP kinases and cell death. Biochem Pharmacol *116*, 1-10. 10.1016/j.bcp.2016.03.009.

83. Belenguer, G., Duart-Abadia, P., Jordan-Pla, A., Domingo-Muelas, A., Blasco-Chamarro, L., Ferron, S.R., Morante-Redolat, J.M., and Farinas, I. (2021). Adult Neural Stem Cells Are Alerted by Systemic Inflammation through TNF-alpha Receptor Signaling. Cell Stem Cell *28*, 285-299 e289. 10.1016/j.stem.2020.10.016.

84. Coppe, J.P., Desprez, P.Y., Krtolica, A., and Campisi, J. (2010). The senescence-associated secretory phenotype: the dark side of tumor suppression. Annu Rev Pathol *5*, 99-118. 10.1146/annurev-pathol-121808-102144.
85. Munoz-Fontela, C., Macip, S., Martinez-Sobrido, L., Brown, L., Ashour, J., Garcia-Sastre, A., Lee, S.W., and Aaronson, S.A. (2008). Transcriptional role of p53 in interferon-mediated antiviral immunity. J Exp Med *205*, 1929-1938. 10.1084/jem.20080383.
86. Schauder, D.M., Shen, J., Chen, Y., Kasmani, M.Y., Kudek, M.R., Burns, R., and Cui, W. (2021). E2A-regulated epigenetic landscape promotes memory CD8 T cell differentiation. Proc Natl Acad Sci U S A *118*. 10.1073/pnas.2013452118.
87. Kandhaya-Pillai, R., Miro-Mur, F., Alijotas-Reig, J., Tchkonia, T., Kirkland, J.L., and Schwartz, S. (2017). TNFalpha-senescence initiates a STAT-dependent positive feedback loop, leading to a sustained interferon signature, DNA damage, and cytokine secretion. Aging (Albany NY) *9*, 2411-2435. 10.18632/aging.101328.
88. Van de Sande, B., Flerin, C., Davie, K., De Waegeneer, M., Hulselmans, G., Aibar, S., Seurinck, R., Saelens, W., Cannoodt, R., Rouchon, Q., et al. (2020). A scalable SCENIC workflow for single-cell gene regulatory network analysis. Nat Protoc *15*, 2247-2276. 10.1038/s41596-020-0336-2.
89. Factor, D.C., Barbeau, A.M., Allan, K.C., Hu, L.R., Madhavan, M., Hoang, A.T., Hazel, K.E.A., Hall, P.A., Nisraiyya, S., Najm, F.J., et al. (2020). Cell Type-Specific Intralocus Interactions Reveal Oligodendrocyte Mechanisms in MS. Cell *181*, 382-395 e321. 10.1016/j.cell.2020.03.002.
90. International Multiple Sclerosis Genetics, C., and Multiple, M.S.C. (2023). Locus for severity implicates CNS resilience in progression of multiple sclerosis. Nature *619*, 323-331. 10.1038/s41586-023-06250-x.
91. Unnikrishnan, A., Hadad, N., Masser, D.R., Jackson, J., Freeman, W.M., and Richardson, A. (2018). Revisiting the genomic hypomethylation hypothesis of aging. Ann N Y Acad Sci *1418*, 69-79. 10.1111/nyas.13533.
92. Campagna, M.P., Xavier, A., Lea, R.A., Stankovich, J., Maltby, V.E., Butzkueven, H., Lechner-Scott, J., Scott, R.J., and Jokubaitis, V.G. (2022). Whole-blood methylation signatures are associated with and accurately classify multiple sclerosis disease severity. Clin Epigenetics *14*, 194. 10.1186/s13148-022-01397-2.
93. Roy, E., and Cao, W. (2022). Glial interference: impact of type I interferon in neurodegenerative diseases. Mol Neurodegener *17*, 78. 10.1186/s13024-022-00583-3.
94. Rasa, S.M.M., Annunziata, F., Krepelova, A., Nunna, S., Omrani, O., Gebert, N., Adam, L., Kappel, S., Hohn, S., Donati, G., et al. (2022). Inflammaging is driven by upregulation of innate immune receptors and systemic interferon signaling and is ameliorated by dietary restriction. Cell Rep *39*, 111017. 10.1016/j.celrep.2022.111017.
95. Gulen, M.F., Samson, N., Keller, A., Schwabenland, M., Liu, C., Gluck, S., Thacker, V.V., Favre, L., Mangeat, B., Kroese, L.J., et al. (2023). cGAS-STING drives ageing-related inflammation and neurodegeneration. Nature *620*, 374-380. 10.1038/s41586-023-06373-1.
96. Tabula Muris, C. (2020). A single-cell transcriptomic atlas characterizes ageing tissues in the mouse. Nature *583*, 590-595. 10.1038/s41586-020-2496-1.
97. Xie, X., Ma, G., Li, X., Zhao, J., Zhao, Z., and Zeng, J. (2023). Activation of innate immune cGAS-STING pathway contributes to Alzheimer's pathogenesis in 5xFAD mice. Nat Aging *3*, 202-212. 10.1038/s43587-022-00337-2.

98. Standaert, D.G., and Childers, G.M. (2022). Alpha-synuclein-mediated DNA damage, STING activation, and neuroinflammation in Parkinson's disease. Proc Natl Acad Sci U S A *119*, e2204058119. 10.1073/pnas.2204058119.
99. Levine, K.S., Leonard, H.L., Blauwendraat, C., Iwaki, H., Johnson, N., Bandres-Ciga, S., Ferrucci, L., Faghri, F., Singleton, A.B., and Nalls, M.A. (2023). Virus exposure and neurodegenerative disease risk across national biobanks. Neuron *111*, 1086-1093 e1082. 10.1016/j.neuron.2022.12.029.
100. Bjornevik, K., Cortese, M., Healy, B.C., Kuhle, J., Mina, M.J., Leng, Y., Elledge, S.J., Niebuhr, D.W., Scher, A.I., Munger, K.L., and Ascherio, A. (2022). Longitudinal analysis reveals high prevalence of Epstein-Barr virus associated with multiple sclerosis. Science *375*, 296-301. 10.1126/science.abj8222.
101. Wilkins, J.M., Gakh, O., Kabiraj, P., McCarthy, C.B., Tobin, W.O., Howe, C.L., and Lucchinetti, C.F. (2020). Signatures of cell stress and altered bioenergetics in skin fibroblasts from patients with multiple sclerosis. Aging (Albany NY) *12*, 15134-15156. 10.18632/aging.103612.
102. Kury, P., Nath, A., Creange, A., Dolei, A., Marche, P., Gold, J., Giovannoni, G., Hartung, H.P., and Perron, H. (2018). Human Endogenous Retroviruses in Neurological Diseases. Trends Mol Med *24*, 379-394. 10.1016/j.molmed.2018.02.007.
103. Garza, R., Sharma, Y., Atacho, D.A.M., Thiruvalluvan, A., Abu Hamdeh, S., Jonsson, M.E., Horvath, V., Adami, A., Ingelsson, M., Jern, P., et al. (2023). Single-cell transcriptomics of human traumatic brain injury reveals activation of endogenous retroviruses in oligodendroglia. Cell Rep *42*, 113395. 10.1016/j.celrep.2023.113395.
104. Lin, B., Coleman, J.H., Peterson, J.N., Zunitch, M.J., Jang, W., Herrick, D.B., and Schwob, J.E. (2017). Injury Induces Endogenous Reprogramming and Dedifferentiation of Neuronal Progenitors to Multipotency. Cell Stem Cell *21*, 761-774 e765. 10.1016/j.stem.2017.09.008.
105. Absinta, M., Sati, P., Masuzzo, F., Nair, G., Sethi, V., Kolb, H., Ohayon, J., Wu, T., Cortese, I.C.M., and Reich, D.S. (2019). Association of Chronic Active Multiple Sclerosis Lesions With Disability In Vivo. JAMA Neurol *76*, 1474-1483. 10.1001/jamaneurol.2019.2399.
106. Preziosa, P., Pagani, E., Meani, A., Moiola, L., Rodegher, M., Filippi, M., and Rocca, M.A. (2022). Slowly Expanding Lesions Predict 9-Year Multiple Sclerosis Disease Progression. Neurol Neuroimmunol Neuroinflamm *9*. 10.1212/NXI.0000000000001139.
107. Douvaras, P., and Fossati, V. (2015). Generation and isolation of oligodendrocyte progenitor cells from human pluripotent stem cells. Nat Protoc *10*, 1143-1154. 10.1038/nprot.2015.075.
108. Ewels, P., Magnusson, M., Lundin, S., and Kaller, M. (2016). MultiQC: summarize analysis results for multiple tools and samples in a single report. Bioinformatics *32*, 3047-3048. 10.1093/bioinformatics/btw354.
109. Shen, W., Le, S., Li, Y., and Hu, F. (2016). SeqKit: A Cross-Platform and Ultrafast Toolkit for FASTA/Q File Manipulation. PLoS One *11*, e0163962. 10.1371/journal.pone.0163962.
110. Mohorianu, I., Bretman, A., Smith, D.T., Fowler, E.K., Dalmay, T., and Chapman, T. (2017). Comparison of alternative approaches for analysing multi-level RNA-seq data. PLoS One *12*, e0182694. 10.1371/journal.pone.0182694.
111. Dobin, A., Davis, C.A., Schlesinger, F., Drenkow, J., Zaleski, C., Jha, S., Batut, P., Chaisson, M., and Gingeras, T.R. (2013). STAR: ultrafast universal RNA-seq aligner. Bioinformatics *29*, 15-21. 10.1093/bioinformatics/bts635.

112. Liao, Y., Smyth, G.K., and Shi, W. (2014). featureCounts: an efficient general purpose program for assigning sequence reads to genomic features. Bioinformatics *30*, 923-930. 10.1093/bioinformatics/btt656.
113. Danecek, P., Bonfield, J.K., Liddle, J., Marshall, J., Ohan, V., Pollard, M.O., Whitwham, A., Keane, T., McCarthy, S.A., Davies, R.M., and Li, H. (2021). Twelve years of SAMtools and BCFtools. Gigascience *10*. 10.1093/gigascience/giab008.
114. Bolstad, B.M., Irizarry, R.A., Astrand, M., and Speed, T.P. (2003). A comparison of normalization methods for high density oligonucleotide array data based on variance and bias. Bioinformatics *19*, 185-193. 10.1093/bioinformatics/19.2.185.
115. Huynh-Thu, V.A., Irrthum, A., Wehenkel, L., and Geurts, P. (2010). Inferring regulatory networks from expression data using tree-based methods. PLoS One *5*. 10.1371/journal.pone.0012776.
116. Almende, B., Thieurmel, B., and Robert, T. (2019). Package 'visnetwork'.
117. Joglekar, M.V., Satoor, S.N., Wong, W.K.M., Cheng, F., Ma, R.C.W., and Hardikar, A.A. (2020). An Optimised Step-by-Step Protocol for Measuring Relative Telomere Length. Methods Protoc *3*. 10.3390/mps3020027.
118. Kechin, A., Boyarskikh, U., Kel, A., and Filipenko, M. (2017). cutPrimers: A New Tool for Accurate Cutting of Primers from Reads of Targeted Next Generation Sequencing. J Comput Biol *24*, 1138-1143. 10.1089/cmb.2017.0096.
119. Kim, D., Paggi, J.M., Park, C., Bennett, C., and Salzberg, S.L. (2019). Graph-based genome alignment and genotyping with HISAT2 and HISAT-genotype. Nat Biotechnol *37*, 907-915. 10.1038/s41587-019-0201-4.
120. Krueger, F., and Andrews, S.R. (2011). Bismark: a flexible aligner and methylation caller for Bisulfite-Seq applications. Bioinformatics *27*, 1571-1572. 10.1093/bioinformatics/btr167.
121. Akalin, A., Kormaksson, M., Li, S., Garrett-Bakelman, F.E., Figueroa, M.E., Melnick, A., and Mason, C.E. (2012). methylKit: a comprehensive R package for the analysis of genome-wide DNA methylation profiles. Genome Biol *13*, R87. 10.1186/gb-2012-13-10-r87.
122. Juhling, F., Kretzmer, H., Bernhart, S.H., Otto, C., Stadler, P.F., and Hoffmann, S. (2016). metilene: fast and sensitive calling of differentially methylated regions from bisulfite sequencing data. Genome Res *26*, 256-262. 10.1101/gr.196394.115.
123. McCullagh, P., and Nelder, J.A. (1998). Generalized linear models, 2nd Edition (Chapman & Hall/CRC).
124. Heinz, S., Benner, C., Spann, N., Bertolino, E., Lin, Y.C., Laslo, P., Cheng, J.X., Murre, C., Singh, H., and Glass, C.K. (2010). Simple combinations of lineage-determining transcription factors prime cis-regulatory elements required for macrophage and B cell identities. Mol Cell *38*, 576-589. 10.1016/j.molcel.2010.05.004.
125. Ying, K., Tyshkovskiy, A., Trapp, A., Liu, H., Moqri, M., Kerepesi, C., and Gladyshev, V.N. (2023). ClockBase: ClockBase: a comprehensive platform for biological age profiling in human and mouse. bioRxiv. https://doi.org/10.1101/2023.02.28.530532.
126. Hao, Y., Hao, S., Andersen-Nissen, E., Mauck, W.M., 3rd, Zheng, S., Butler, A., Lee, M.J., Wilk, A.J., Darby, C., Zager, M., et al. (2021). Integrated analysis of multimodal single-cell data. Cell *184*, 3573-3587 e3529. 10.1016/j.cell.2021.04.048.
127. Korsunsky, I., Millard, N., Fan, J., Slowikowski, K., Zhang, F., Wei, K., Baglaenko, Y., Brenner, M., Loh, P.R., and Raychaudhuri, S. (2019). Fast, sensitive and accurate integration of single-cell data with Harmony. Nat Methods *16*, 1289-1296. 10.1038/s41592-019-0619-0.

128. Kolberg, L., Raudvere, U., Kuzmin, I., Vilo, J., and Peterson, H. (2020). gprofiler2 -- an R package for gene list functional enrichment analysis and namespace conversion toolset g:Profiler. F1000Res *9*. 10.12688/f1000research.24956.2.
129. Hafemeister, C., and Satija, R. (2019). Normalization and variance stabilization of single-cell RNA-seq data using regularized negative binomial regression. Genome Biol *20*, 296. 10.1186/s13059-019-1874-1.
130. Qiu, X., Mao, Q., Tang, Y., Wang, L., Chawla, R., Pliner, H.A., and Trapnell, C. (2017). Reversed graph embedding resolves complex single-cell trajectories. Nat Methods *14*, 979-982. 10.1038/nmeth.4402.
131. Aibar, S., Gonzalez-Blas, C.B., Moerman, T., Huynh-Thu, V.A., Imrichova, H., Hulselmans, G., Rambow, F., Marine, J.C., Geurts, P., Aerts, J., et al. (2017). SCENIC: single-cell regulatory network inference and clustering. Nat Methods *14*, 1083-1086. 10.1038/nmeth.4463.
132. Wolf, F.A., Angerer, P., and Theis, F.J. (2018). SCANPY: large-scale single-cell gene expression data analysis. Genome Biol *19*, 15. 10.1186/s13059-017-1382-0.
133. Stuart, T., Srivastava, A., Madad, S., Lareau, C.A., and Satija, R. (2021). Single-cell chromatin state analysis with Signac. Nat Methods *18*, 1333-1341. 10.1038/s41592-021-01282-5.
134. Granja, J.M., Corces, M.R., Pierce, S.E., Bagdatli, S.T., Choudhry, H., Chang, H.Y., and Greenleaf, W.J. (2021). ArchR is a scalable software package for integrative single-cell chromatin accessibility analysis. Nat Genet *53*, 403-411. 10.1038/s41588-021-00790-6.
135. McLean, C.Y., Bristor, D., Hiller, M., Clarke, S.L., Schaar, B.T., Lowe, C.B., Wenger, A.M., and Bejerano, G. (2010). GREAT improves functional interpretation of cis-regulatory regions. Nat Biotechnol *28*, 495-501. 10.1038/nbt.1630.
136. Bravo Gonzalez-Blas, C., De Winter, S., Hulselmans, G., Hecker, N., Matetovici, I., Christiaens, V., Poovathingal, S., Wouters, J., Aibar, S., and Aerts, S. (2023). SCENIC+: single-cell multiomic inference of enhancers and gene regulatory networks. Nat Methods *20*, 1355-1367. 10.1038/s41592-023-01938-4.